9-21-2023

Thermodynamic and Kinetic Modeling of Electrocatalytic Reactions Using a First-Principles Approach

M. Vasanthapandiyan
Shiv Nadar Institution of Eminence

Shagun Singh
Shiv Nadar Institution of Eminence

Fernanda Bononi
University of North Texas

Oliviero Andreussi
Boise State University

Naiwrit Karmodak
Shiv Nadar Institution of Eminence

The Journal of Chemical Physics REVIEW pubs.aip.org/aip/jcp

Thermodynamic and kinetic modeling of electrocatalytic reactions using a first-principles approach

Cite as: J. Chem. Phys. 159, 111001 (2023); doi: 10.1063/5.0165835
Submitted: 30 June 2023 • Accepted: 28 August 2023 •
Published Online: 20 September 2023

Vasanthapandiyan M,[1] Shagun Singh,[1] Fernanda Bononi,[2] Oliviero Andreussi,[3] and Naiwrit Karmodak[1,a)]

AFFILIATIONS

[1] Department of Chemistry, Shiv Nadar Institution of Eminence, Dadri, Gautam Buddha Nagar, Uttar Pradesh 201314, India
[2] Department of Physics, University of North Texas, Denton, Texas 76203, USA
[3] Department of Chemistry and Biochemistry, Boise State University, Boise, Idaho 83725, USA

[a)] **Author to whom correspondence should be addressed:** naiwrit.karmodak@snu.edu.in

ABSTRACT

The computational modeling of electrochemical interfaces and their applications in electrocatalysis has attracted great attention in recent years. While tremendous progress has been made in this area, however, the accurate atomistic descriptions at the electrode/electrolyte interfaces remain a great challenge. The Computational Hydrogen Electrode (CHE) method and continuum modeling of the solvent and electrolyte interactions form the basis for most of these methodological developments. Several posterior corrections have been added to the CHE method to improve its accuracy and widen its applications. The most recently developed grand canonical potential approaches with the embedded diffuse layer models have shown considerable improvement in defining interfacial interactions at electrode/electrolyte interfaces over the state-of-the-art computational models for electrocatalysis. In this Review, we present an overview of these different computational models developed over the years to quantitatively probe the thermodynamics and kinetics of electrochemical reactions in the presence of an electrified catalyst surface under various electrochemical environments. We begin our discussion by giving a brief picture of the different continuum solvation approaches, implemented within the *ab initio* method to effectively model the solvent and electrolyte interactions. Next, we present the thermodynamic and kinetic modeling approaches to determine the activity and stability of the electrocatalysts. A few applications to these approaches are also discussed. We conclude by giving an outlook on the different machine learning models that have been integrated with the thermodynamic approaches to improve their efficiency and widen their applicability.

I. INTRODUCTION

With the rapid development of modern technologies, the world is experiencing a significant increase in energy consumption. This enhanced the dependence on fossil fuels and the continuous increase in carbon dioxide (CO_2) concentration in the atmosphere. Environmental problems, such as rising sea levels, ozone layer depletion, extreme weather patterns, and climate-change-related issues, have endangered the entire ecosystem. To mitigate these issues, in the past few decades, there has been an increase in global interest toward shifting energy production from fossil fuels to renewable and sustainable sources.[1–6]

Among alternative technologies, electrocatalysis and photoelectrocatalysis hold great promise as a means of energy storage, allowing to fully unlock the power of renewable energy sources, such as wind and solar.[7–9] The electrochemical reactions in the water and carbon cycles could serve as critical processes to reduce the dependence on fossil fuels and help reduce atmospheric carbon dioxide emission.[10–13] The electrochemical water splitting reactions will allow the generation of a clean fuel—hydrogen (H_2).[14,15] On the other hand, the electrochemical reactions in the carbon cycles could be used to convert CO_2 to value-added chemicals and fuels.[12,16,17]

Efficient electrocatalysts are needed to meet the industrial scale applications of these reactions. Electrodes made of Pt-group elements are the best electrocatalysts for most of these electrochemical reactions to date.[7,18,19] While a few studies found mixed Ni–Fe oxides as promising electrocatalysts for water electrolyzers under alkaline conditions,[20,21] however, under acidic conditions, RuO_2 and

IrO_2 show the best activity.[22,23] The expensive nature of most of these materials forbids their industrial-scale applications. Therefore, identifying materials composed of earth-abundant materials has acquired immense research interest in the last few years.

However, understanding materials' surface characteristics, stability, and reactivity under electrochemical conditions is challenging. With experimental techniques to probe electrified solid–liquid interfaces still evolving, computational methods could provide an efficient alternative to explore these interfaces' atomistic details and offer design strategies for better electrocatalysts.[24,25] Indeed, a systematic experimental exploration of the interfacial characteristics and chemical reactivity of electrified solid/electrolyte interfaces would be costly and time-consuming. On the other hand, computational approaches could help understand materials' properties and reactivity in a high-throughput fashion and, therefore, guide experiments on the best-performing candidates.

The accuracy of the computer simulations to understand the chemical stability and reactivity of electrode materials is primarily defined by the theoretical strategies used to model the solid surface, adsorbates, solvated ions in the electrolyte, solvent molecules, and the effect of external potential and pH on the electrosorption mechanism at the interface.[26,27] First-principles density functional theory (DFT) calculations have been widely used to accurately define most of these interactions at the solid/electrolyte interface.[27] Periodic DFT calculations with plane-wave basis sets and pseudopotential to model core electrons have successfully enabled the modeling of solid surfaces and their interactions with reactive intermediates in vacuum in several computational electrocatalysis studies.[28] However, the accurate description of solvent molecules and electrolyte ions brings significant complexity.[29,30] An explicit description of the electrolyte solution that accounts for its statistical nature, e.g., through molecular dynamics simulations, would allow the full characterization of the atomistic details of interfacial processes. However, the balance between the accuracy and computational cost of such a fully explicit model makes it only feasible for selected applications, leaving high-throughput screenings out of reach.

A multi-scale approach to defining solvent effects on solid surfaces could reduce these computational challenges.[31,32] Following a hierarchical strategy, a first-principles level of theory that includes full atomistic and electronic details is adopted for the electrode surface and the catalytic adsorbates. Instead, solvent molecules and electrolyte ions are statistically averaged and converted into classical continuum embedding media, their interactions with the substrate being described using empirical or theoretical models. The most common methods in this category follow the name of continuum solvation models and include as one of their key ingredients the description of the solvent media as a classical polarizable dielectric, with variations of the Polarizable Continuum Model of Tomasi and Persico[33] and the SM-X approaches of Truhlar and collaborators[34] being probably the most popular in the computational chemistry literature. At the cost of requiring some careful parameterizations and reducing the details in the characterization of interfacial processes, these continuum embedding models have unlocked the possibility of performing high-throughput calculations on materials surfaces.

In addition to precise computational models to define the simulation setup, accurate thermodynamic models are needed to probe the electron transfer mechanism at the solid/electrolyte interface. The methodological developments contributed by Reuter and Scheffler on heterogeneous catalysis[35,36] and the computational hydrogen electrode (CHE) method[37] put forward by Nørskov and Rossmeisl represent the cornerstones of computational thermodynamics for free energy calculations of electrochemical reactions. The CHE method has reduced the computational efforts and complexities associated with high-throughput screening of a larger set of catalysts for several electrochemical reactions. In recent years, additional corrections based on a Legendre transform formalism have extended the CHE method to efficiently incorporate surface dipole interactions and electric fields, which influence electrosorption free energy values at the electrode/electrolyte interfaces for some electrochemical reactions.[38–41]

In this Review, we will present an overview of the different computational tools and thermodynamic models developed based upon first principles methods to probe the thermodynamics of electrochemical reactions. In the next sections, we describe the computational embedding models for solvent (Sec. III) and electrolytes (Sec. IV) developed to characterize electrocatalytic interfaces. We follow with an overview of *ab* initio methods to probe electrosorption free energy values on electrode surfaces, including the CHE method (Sec. V) and its different *a posteriori* modifications aimed at improving its accuracy and efficiency (Sec. VI). We then provide a discussion on kinetic models developed to characterize kinetic barriers of electrochemical reactions (Sec. VII) and to connect atomistic results with experimental reaction rates (Sec. VIII). In Sec. XI, we report an overview of thermodynamic models to understand the electrochemical stability of wet electrified surfaces under applied potential and pH. Eventually, we conclude our discussion by giving a note on the current scenario and future methodological developments required to enhance the applicability of the computational electrochemical methods.

II. CONTINUUM MODELS FOR SOLUTIONS

Continuum models of solvation are developed based on the basic assumption that the solvent molecules are statistically averaged and homogeneously present around the solvated system (the quantum mechanical systems of interest).[32,33,42,43] Figure 1 shows a schematic representation of the continuum approximation as ideally emerging from full-explicit atomistic solvent models.

For any continuum embedding approach, the definition of the boundary between the solvated system and the surrounding environment is the main component. This interfacial region could be modeled in different ways depending upon the dimension of the embedding region (for two, one, or zero-dimensional systems) and the types of interactions between the solvent molecules and the embedding region. A consistent picture of the interfacial region can be derived in terms of the interface function s(r) given as follows:[33,42]

$$s(r) = \begin{cases} 1, & r \in \text{system}, \\ 0, & r \notin \text{system}. \end{cases}$$

The well-known polarizable continuum model (PCM) relies on an interface function with a sharp transition defined as the union of spheres centered at the positions of the atoms comprising the quantum mechanical region.[42,44–48] In this approach, the interface function is strictly defined in terms of the van-der-Waals radii (R_i^{vdW})

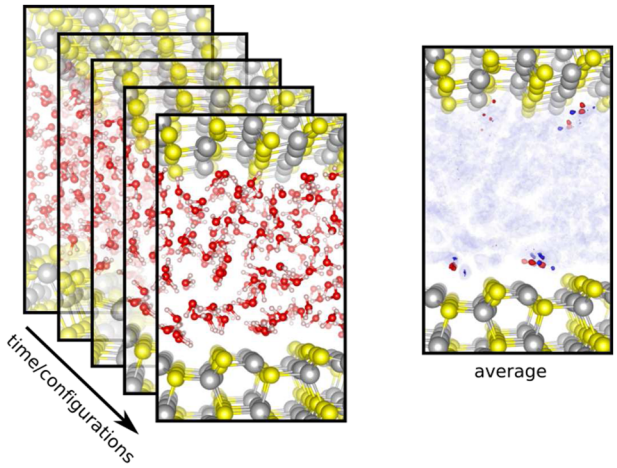

FIG. 1. The continuum solvation representation in comparison to the full-explicit solvent model. The figure is reprinted with permission from O. Andreussi and G. Fisicaro, Int. J. Quantum Chem. **119**, e25725 (2019). Copyright 2019 John Wiley and Sons, Ltd.[31] Different configurations of the explicit water molecules are shown on the GaAs surface in the left panel, wherein in the right panel, an average distribution of the solvent molecules is represented by a continuum medium based upon the probability distribution isosurfaces of the water molecules.

of the atoms of the embedded system, which are element-dependent parameters usually obtained from independent parameterizations. The sharp transition between system and environment regions allows us to recast the numerical problems connected with the calculation of solute–solvent interactions onto the two-dimensional surface of the interface, with significant computational advantages for small isolated systems.

Another important contribution has been made by Klamt and Schüürmann to the development of the solvent model.[49,50] They devised a conductor like solvent model (COSMO) to define the electrostatic interaction of the solute molecule with the solvent. In contrast to the PCM, in this model, the continuum polarization charges due to the solute polarity is derived following a scaled-conductor approximation. The screened surface charge on the solute molecule is denoted by Eq. (1), where q* is the electric surface charge obtained quantum mechanically,

$$q = \frac{\varepsilon - 1}{\varepsilon + x} q^*. \tag{1}$$

The value of x varies between 0.5 and 0.0 for neutral and charged molecules, respectively.

In addition to the parametrization of the solute surfaces, a few solvation models are developed with the parametrization included for the solvent properties. The SMx models developed by Cramer and Truhlar are one of those notable solvation models,[34,51–54] where different widely available solvent descriptors are introduced to model the solute surface interactions, solvent properties, and surface non-electrostatic interactions. These models could enable the solvation strategies of non-aqueous solvents, such as the organic solvents.[54,55]

However, all these solvent approaches can lead to inconsistent errors in quantum mechanical calculations for extended two-dimensional interfaces.[56,57] To build a more transferable continuum solvation model suitable for periodic materials simulations, a smooth-interface approach was introduced by Fisicaro *et al.*[56] in terms of the so-called soft spheres. The resulting soft-sphere continuum solvation (SSCS) model introduced additional smoothing parameters that allow the mapping of the interface function on typical structured grids adopted in plane-wave-based first-principles simulation packages.

Defining the interface function on ionic degrees of freedom neglects changes in solvation geometries linked to the electronic degrees of freedom, e.g., during charge-transfer processes.[56,58] Moreover, the explicit dependence of the interface function on ionic positions introduces additional contributions to the inter-atomic forces. Therefore, a lack of sufficient numerical accuracy in the calculation of solvent-interaction terms may propagate to the poorly converged forces, with potential issues in geometry optimizations and poor energy conservation in micro-canonical molecular dynamics simulations. When appropriately parameterized, sharp-interface models (such as PCM and SM-X family of approaches) or smooth-interface models have shown similar accuracies for neutral and charged organic molecules in solution, with the best-performing models usually relying on additional parameters to capture specific interactions (e.g., hydrogen bonds) usually overlooked by the continuum assumption. In particular, in models whose interface is based on atom-centered spheres, the accuracy may be improved by accurately adjusting the scaling parameters to define the solvation radii of the different molecular functional groups and charged surfaces. Nevertheless, accurate *a priori* knowledge of solvent interactions with the individual components of the system is required in order to accurately tune the scaling factors.[56]

An alternative approach to model the solvation interface is based on the electronic density of the embedded system,

$$s(r) \equiv s(\rho^{el}(r)). \tag{2}$$

By introducing a formal connection between the interface function and the electronic density of the embedded system, the shape of the continuum interface gets updated at every self-consistent field (SCF) cycle and, therefore, automatically accounts for changes in the electronic charge distribution.[31,59–62] While this flexible adjustment of the interface may appear to provide a more physical description of solvation geometries, the approach leads to a non-physical expansion of the interface function for the negatively charged systems.[63,64] Nonetheless, sharp-interface models (IPCM and SCIPCM)[65] and smooth-interface models (Fattebert and Gygi, SCCS, etc.)[29,43,59,62,64,66] based on the electronic density have the main advantage of providing an interface function that is more general and transferable as it does not require van der Waals radii and is thus independent of the types of elements present in the simulation. This can represent a key advantage when studying systems such as materials based on transition metals, in which most of the atoms belong to elements that are not well represented in the organic compounds traditionally used for solvation model parameterization. As a second minor advantage, due to the Hellmann–Feynman theorem, continuum interfaces defined on the electronic density

alone do not add explicit contributions to interatomic forces. Ideally, these solvation models are more well-behaved for molecular dynamics simulations.[59] However, when the interface function is defined in terms of the ionic positions, an additional contribution to the interatomic forces linked to the variation of the interface with respect to the ionic positions need to be explicitly included. In specific instances, the dependence on ionic positions can be designed so as to not affect the energy and, correspondingly, the forces, e.g., when adding a fictitious core-electron density to saturate the interface function on the position of the ions. However, in most cases, this additional contribution needs to be computed explicitly, and numerical inaccuracies linked to the discretization of the interface may lead to increased errors in the forces, potentially limiting the application of these methods to molecular dynamics simulations.

Among the different interface models based on the electronic density, it is worth mentioning the revised definition formulated by Andreussi and co-workers, denoted as the self-consistent continuum solvation (SCCS), and exploiting a physically motivated definition of the switching function, given as follows:[59]

$$s(r) = \begin{cases} 1, & \rho^{el}(\mathrm{r}) > \rho_{\max}, \\ f(\ln(\rho^{el}(\mathrm{r}))), & \rho_{\max} > \rho^{el}(\mathrm{r}) > \rho_{\min}, \\ 0, & \rho^{el}(\mathrm{r}) < \rho_{\min}, \end{cases}$$

where $f(\ln(\rho^{el}(\mathrm{r})))$ is a smoothly varying function of the logarithm of the electronic density. Using a piece-wise definition is instrumental in ensuring that the polarization charge induced in the continuum is not too close to the system's degrees of freedom. Moreover, the use of the logarithm of the electronic density, in a region of space where the electronic density is known to decay exponentially, is crucial to ensure the numerical stability and efficiency of the approach. The interface function depends upon two parameters, $\rho_{\min}$ and $\rho_{\max}$, corresponding to two iso-surfaces of the electron density of the embedded region. A higher value of these parameters denotes that the interface is closer to the quantum mechanical region and that solute–solvent interactions are stronger. Lower values push the solvation threshold away from the quantum mechanical region, thereby reducing solvent effects.

Figure 2 shows a comparison between two smooth-interface continuum models based on the ionic (SSCS) or electronic (SCCS) degrees of freedom of the system, visualized for a Pt slab with a hydroxyl group adsorbed on the surface. For both models, the minimal number of model parameters, and, in particular, the cavity parameters that control the position and the smoothness of the interface with respect to the system, were determined so as to optimize the values of solvation free energies of small organic molecules in water as compared to the experiments. Despite the differences in the shapes of the two interfaces, when the appropriate parameterization is performed, both models show similar accuracy and similar effects on the solvated systems.[63,64]

The calculations on a comprehensive set of neutral molecules showed that by tuning these two parameters, the solvent interactions could be effectively defined and can reproduce the results in a similar agreement with other theoretical solvent models or the experiments.[63,64] The solvent interactions with the cationic systems defined with these parameters are represented well, whereas the anionic systems show significant discrepancies. In addition to the

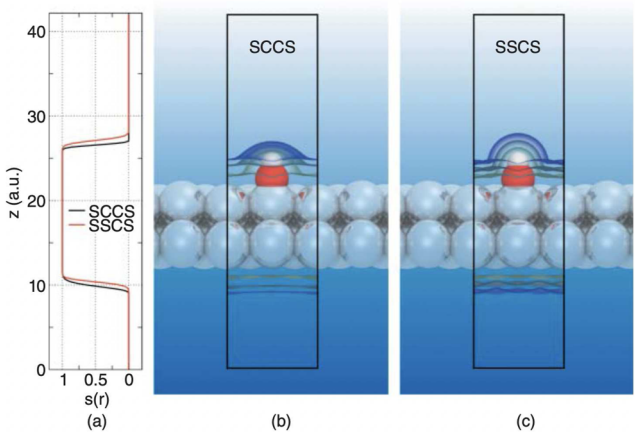

FIG. 2. (a) The behavior of the interface functions with the SCCS and SSCS model for a hydroxide adsorbed Pt (111) surface. The continuum-embedded interfaces of the Pt(111) surface with a hydroxide ion adsorbed modeled using the SCCS and SSCS models are represented in (b) and (c), respectively. The lines in panel (a) represent the values of the SCCS and SSCS interface functions along a line oriented perpendicular to the slab and passing through the oxygen atom. The specific behavior of these functions changes significantly as one moves along the plane of the slab. However, from the figure, it is clear that both interfaces are flat (have zero derivative) in most of the simulation space while varying very sharply in a small region of space at about the same distance from the atoms of the system. The figure is taken from Andreussi, Nattino, and Georg Hörmann, *Atomic-Scale Modelling of Electrochemical Systems.* Copyright 2021 John Wiley and Sons.[67]

molecular systems, the cavity parametrizations are also performed for the electrochemical interfaces.[68] An alternative set of electron density parameters are found to be more suitable while studying electrochemical interfaces with continuum solvation. These parameters are found to effectively represent the potential of zero charge values and differential capacitance for the noble metal surfaces[38] and the aqueous solvent interactions of the two-dimensional surfaces.[69]

However, it is observed that errors in interface threshold parametrizations can lead to unrealistic simulation results. To assess accurate solvation effects on molecular solutes, the usage of parametrization from molecular reference data is important. Therefore, it could be challenging to determine electrochemical interfacial surfaces and reaction energetics for systems without a prior research data. The over-structure of the solvation layers, particularly for the ionic systems, found out to be the main concerns associated with most of the implicit solvent models.

To overcome some of these issues with the ionic solutes, non-local interfaces depending upon both the ionic and electronic degrees of freedom have been developed. A field-aware interface, where scaling factor proportional to local electrostatic fields of the system, has been introduced to model the non-local electrostatic interactions at the solute–solvent interfaces for ionic systems.[70]

A second limitation that has been observed with the ionic and electronic interfaces is the unphysical distribution of continuum solvent to small regions of space inaccessible to solute molecules. This causes serious limitations to complex systems, such as the open or porous substances and zeolites, where interstitial spaces are present between different solute molecules or the surface and the adsorbates. To address this issue, a solvent-aware definition of continuum

interfaces is proposed, which uses convolutions with spherical functions to reduce the continuum embedding within the inaccessible regions.[64] The local interface function s(r) discussed above is complemented with a smooth switching function of the fraction of the space occupied by the embedding medium within the spherical region.

With the non-local solvent interfaces, extensive improvements could be achieved in geometry minimizations and molecular dynamics simulations; however, these embedding approaches lack precise modeling of specific solute–solvent interactions beyond the continuum approximation. For example, the interfacial H-bond interactions between the protic solvents and the charged electrode surfaces with and without the reactive intermediates could not be extensively defined using these embedding models.[71] Hybrid approaches, where the electrochemical interfaces are modeled by combining the implicit and explicit solvent models, are found to hold potential advantages in providing accurate simulation results with respect to the experiments.[72–74]

A simplified approach to hybrid implicit/explicit solvent modeling has been developed using the quantum mechanical/molecular mechanical (QM/MM) approach. The QM region incorporates the solid electrode and the reaction intermediates thereon, whereas a MM region based upon the force-fields or interatomic potentials is defined for the liquid electrolyte. This approach offers a speedup of simulation time along the same line with the classical dynamics. However, the classical description of electrolyte medium is unable to define the specific interactions (such as the H-bond interactions) between the electrode/electrolyte interfaces, particularly when the liquid phase actively effects the reaction mechanism. This limitation can, however, be mitigated by including a quantum definition of the liquid layer with the *ab initio* molecular dynamics (AIMD) simulations to determine the solvent molecular arrangements.

While QM/MM or full QM description of the hybrid implicit/explicit solvent model greatly simplifies the computational modeling of liquid-medium, nevertheless accurate sampling of the liquid medium would need rigorous molecular dynamics simulations to determine the solvent configurations. To remove the sample-space dependence on the simulation setups, a further coarse-graining step has been introduced by averaging out the movement of the liquid and ionic movements using a spatially equilibrium distribution function employed with the reference interaction site model (RISM) for solvation.[75,76] The equilibrium structure of the solvent molecules around the solute is defined using an analytical integral function denoted as the Ornstein–Zernike equation.[77,78] The rotationally averaged spatial functions lacks the three-dimensional representation of the solvent molecules; therefore, central pair correlation functions on a three-dimensional grid centered around the solute molecule have been introduced. This formalism is denoted as the 3D-RISM method.[79]

The spatial distribution functions in RISM approach is integrated over space and yields an excess chemical potential due to the solute–solvent interactions and solvent reorganization in the presence of solute. The functional derivative with respect to the electron density gives the effective potential, which could be included into the solvent Hamiltonian to determine the electrostatic, dispersion, and exchange interaction terms due to the solvation. Later, Otani and co-workers combined the RISM method with the plane-wave pseudo potentials (PW-PP) to develop the hybrid solvation model to capture the electrostatic interactions at the periodic surfaces.[80,81]

While the accuracy of these hybrid solvent models will be higher than the full implicit models, the cost of these calculations would increase as the size of the simulation setup grows.

III. CONTINUUM DIFFUSE-LAYER ELECTROLYTE MODELS

Along with the definitions of the solvent effects, to accurately define the electrode/electrolyte interface, the embedding framework should also incorporate the effect of electrolyte ions present in the solvating medium.[62,82] This could be defined by using smooth functions that depend upon the local concentrations of the solvated ions at the interfacial region and the bulk solvent. Using the interface function s(r) introduced earlier, the electrolyte domain can be defined in terms of the ion-exclusion function $\gamma(r)$, with

$$\gamma(r) = 1 - s(r). \tag{3}$$

Classical continuum models of the electrolyte charge distribution are particularly important to characterize the electrostatic field at the interface of charged electrode surfaces. As charge carriers (electrons or holes) start accumulating on a material, counter-ions from the electrolyte solution are attracted and accumulate near the electrode–electrolyte interface. A first-order approximation to the resulting electrostatic potential could be obtained in terms of a planar charged layer of counter-ions placed parallel to the electrode surface (Helmholtz plane),[83] giving a rigid and well-confined double-layer structure for the electrode/electrolyte interface. From the computational point of view, such a planar counter-charge layer can be modeled using a planar 2D-periodic charge distribution with a Gaussian envelope given as follows:

$$\rho_{ions} = Ae^{-\frac{(x-x_0)^2}{\Delta^2}}, \tag{4}$$

where A is the normalization factor that ensures that the electrolyte charge density fully compensates for the electrode charge, while x_0 and Δ denote the center and width of the electrolyte charge distribution, respectively.

While the Helmholtz double-layer model corresponds to the ground state solution for the charge distribution as the temperature of the system goes to 0 K, it only allows accounting for concentration and temperature effects by empirically adjusting the position of the rigid counter-charge layer with respect to the electrode surface. A more realistic model is developed following the Gouy–Chapman model of the diffuse layer,[84,85] which involves solving a Poisson–Boltzmann equation that features a continuum charge distribution due to the electrolyte ions.[40,68,86] This approach allows us to explicitly introduce temperature and concentration effects into the charge distribution of the electrolyte ions by complementing the electrostatic free energy functional with the solution entropy functional, $S\{C_i(r)\}$, defined as

$$S\{C_i(r)\} = -k_B \sum C_i(r) \ln\left(\frac{C_i(r)}{\gamma(r)}\right), \tag{5}$$

where $C_i(r)$ is the concentration of the electrolyte ions in space for each ion type *i*. By minimizing the total free energy functional of the

electrolyte solution with respect to the involved degrees of freedom, an analytical connection between the ions concentrations and the electrostatic potential, $\phi(r)$m, is obtained, which for the standard Poisson–Boltzmann (PB) problem results in

$$C_i(r) = \gamma(r) C_i^0 e^{-\frac{z_i \phi(r)}{k_B T}}, \tag{6}$$

where C_i^0 is the constant bulk concentration of electrolyte ions, Z_i is the ionic charge of the ith electrolyte species, k_B is the Boltzmann factor, and T is the temperature.

For electrostatic interactions much smaller than the thermal energy, the Boltzmann factor in Eq. (6) can be simplified into a linear dependence on the potential. This is denoted as Linear Poisson–Boltzmann equation (LPB),

$$C_i(r) \approx \gamma(r) C_i^0 \left(1 - \frac{z_i \phi(r)}{k_B T}\right). \tag{7}$$

However, both the standard PB or LPB models can lead to the over-crowding of the electrolyte ions near highly charged systems. This is due to the implicit treatment of these ions as point charges in the formulation of the Gouy–Chapman model. To overcome this limitation, replacing the point-charge approximation of the electrolyte ion distribution to account for the finite size of these ions can provide a significant increase in model accuracy.[68,87,88] Following the derivation of Borukhov *et al.*, an expression for the entropy density and the local concentration of the electrolyte ions in size-modified Poisson Boltzmann (MPBE) model is exploited,

$$S\{C_i(r)\} = -k_B \sum C_i(r) \ln\left(\frac{C_i(r)}{C_{\max}\gamma(r)}\right) - k_B\left(C_{\max}\gamma(r) - \sum C_i(r)\right)\ln\left(1 - \sum \frac{C_i(r)}{C_{\max}\gamma(r)}\right), \tag{8}$$

which leads to more regular dependence of the electrolyte concentration on the electrostatic potential in the system,

$$C_i(r) = \frac{\gamma(r) C_i^0 e^{-\frac{z_i \phi(r)}{k_B T}}}{1 - \sum_i \frac{C_i^0}{C_{\max}}\left(1 - e^{-\frac{z_i \phi(r)}{k_B T}}\right)}. \tag{9}$$

In this model, the additional $C_{\max}$ parameters correspond to the maximum concentration of the electrolyte ions that can accumulate in a volume unit. Following simple geometrical arguments, this value can be directly connected to the effective radius, r_i, of the electrolyte ions. In the limit of $C_{\max} \to \infty$ or for $r_i \to 0$, the MPBE model reduces to the standard PB model.

In addition to introducing size effects, more detailed models can be introduced in order to capture different interaction strengths between the electrode and the electrolyte ions, e.g., to mimic preferential absorption of anions or to capture different ion-surface separations related to the presence of strong solvation shells on specific electrolyte ion types.[89,90]

Differential capacitance curves calculated using the different diffuse layer models for Ag (111) surface are shown in Fig. 3(c). In the Helmholtz double-layer model, the curve is independent of the bulk electrolyte concentration. The linearized and non-linear PB models instead show a clear dependence on the bulk electrolyte concentration. Comparing the different electrolyte models in Fig. 3(c), the non-linear PB models show better agreement with the experimental curves.

IV. IMPLEMENTATION OF EMBEDDING MODELS IN DFT CALCULATIONS

Embedding effects can be incorporated into the simulation of quantum mechanical systems by extending the energy functional of the system into a free energy functional that accounts for system–environment interactions,

$$E^{tot}[\rho^{el}] \to G^{tot}[\rho^{el}] = T[\rho^{el}] + E^{xc}[\rho^{el}] + G^{elec}[\rho^{el}] + G^{non-elec}[\rho^{el}], \tag{10}$$

where the kinetic energy functional, T, and exchange–correlation term, E^{xc}, have their standard meaning as for DFT simulations for systems in vacuum, while the electrostatic energy functional, G^{elec}, accounts for the characteristics of the embedding medium (dielectric permittivity, electrolyte concentration, etc.), and the additional $G_{non-elec}$ term is introduced to model other non-electrostatic system–environment interactions.

In particular, given the definitions above for the entropy of the continuum medium as a function of electrolyte concentrations [Eqs. (5) and (8)], the free energy of a dielectric medium with a finite electrolyte concentration can be written as[68,87]

$$G^{el}[\rho^{el}] = \int \left(\rho^{tot}(r)\phi(r) - \frac{\varepsilon(r)}{8\pi}|\nabla\phi(r)|^2 - \sum_i \mu_i C_i(r) - TS\{C_i(r)\}\right) dr, \tag{11}$$

where the total charge density of the system includes both electrons and nuclei, $\rho^{tot} = \rho^{el} + \rho^{nucl}$, $\varepsilon(r)$ is the dielectric permittivity in the simulation cell, and μ_i is the chemical potential of the electrolyte ions of type i. For a system in vacuum and in the absence of an electrolyte distribution, the formula above simplifies to give rise to the standard electrostatic interactions between the charges of the systems (i.e., electrons–electrons, nuclei–nuclei, and electrons–nuclei). In such a case, the electrostatic potential in space, $\phi[\rho(r)]$, is obtained from $\rho^{tot}(r)$ by solving the standard Poisson equation, $\nabla^2\phi[\rho^{tot}(r)] = -4\pi\rho^{tot}(r)$. However, in the presence of a continuum dielectric medium, the generalized Poisson equation needs to be solved,

$$\nabla.\varepsilon(r)\nabla\phi[\rho^{tot}(r)] = -4\pi\rho^{tot}(r). \tag{12}$$

While in the presence of electrolyte ions, the potential becomes the solution of the full Poisson–Boltzmann equation,

$$\nabla.\varepsilon\nabla\phi[\rho^{tot}(r)] = -4\pi\left(\rho^{tot}(r) + \rho^{ions}(r)\right), \tag{13}$$

with

$$\rho^{ions}(r) = \gamma(r) e N_A \sum_i Z_i C_i(r) \tag{14}$$

in terms of the concentrations C_i defined in Eqs. (6) and (7) or Eq. (9), depending on whether a linearized and/or size-modified model is adopted.

Several numerical approaches have been explored to solve the above differential equations, varying depending on the underlying

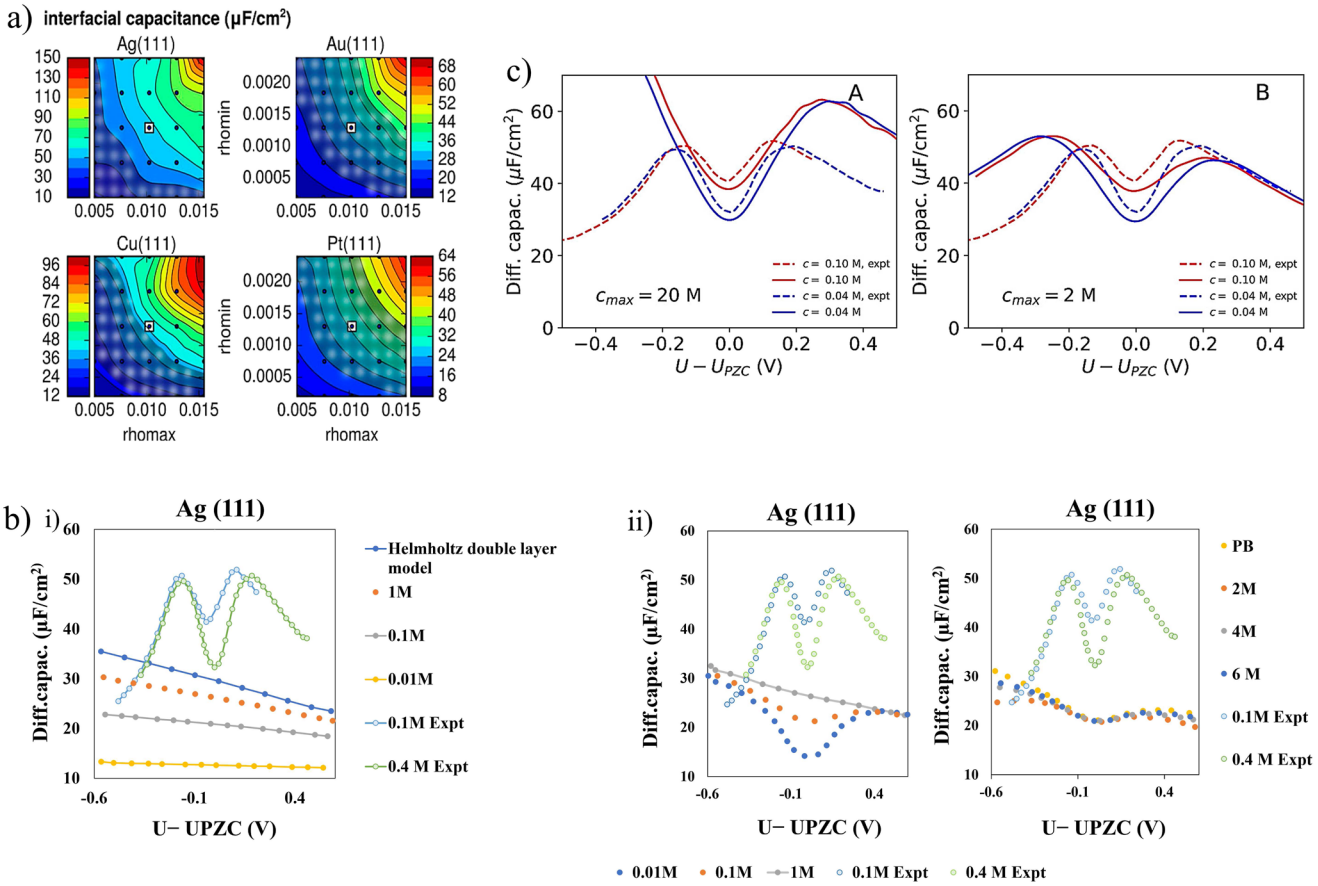

FIG. 3. (a). Dependence of interfacial capacitance of Ag (111), Cu (111), and Pt (111) for the different values of ρ_{min} and ρ_{max}, reproduced from Hörmann, Andreussi, and Marzari, J. Chem. Phys. **150**, 041730 (2019) with the permission of AIP Publishing (b) Differential capacitance of Ag(111) surfaces as a function of applied potential, calculated using different diffuse-layer electrolyte models. (i) Differential capacitance values are calculated using linearized Poisson–Boltzmann (LPB) models (yellow, gray, and orange lines for different electrolyte concentrations) and the double-layer Helmholtz model (blue line). In the double-layer Helmholtz model, the planar counter-charge plane is placed at 5 Å from the outermost metal layer, and the spread parameter is Δ = 0.25 Å. (ii) Differential capacitance behaviors for the nonlinear Poisson–Boltzmann model (left panel with indicated electrolyte concentration) and the size-modified Poisson–Boltzmann model (right panel with the indicated C_{max} values in orange, gray, and blue with a bulk ionic concentration, c_0 of 0.1M). The yellow line corresponds to PB with $C_{max} = \infty$ M). In (b) (i) and (ii), blue-gray and light green lines with respective to 0.1 and 0.4M experimental results, respectively,. (c) Differential capacitance curves for nonlinear size-modified Poisson–Boltzmann models with c_0 = 0.1M using the SSCS [(a), upper panel] and SCCS [(b), lower panel] solvent model. The dashed line represents the experimental data. The C_{max} parameter connected to the size-modified model is set to 20M for SSCS calculations, whereas for the SCCS simulations, a C_{max} value of 2M is considered. The bulk ionic concentration is varied and indicated in the figure. This figure is reprinted from Nattino *et al.*, J. Chem. Phys. **150**, 041722 (2019) with the permission of AIP Publishing.

DFT simulation package and its available Poisson solvers. While multigrid solvers have been initially proposed and specifically developed for this task,[43] fixed-point iterations[59] and preconditioned conjugate gradient approaches[56] based on fast Fourier transforms have shown to be sufficiently accurate and fast for linear electrostatic problems, especially when appropriate periodic-boundary correction schemes are included.[91] For the non-linear Poisson–Boltzmann problems in Eq. (13), Newton-like algorithms were shown to provide reasonably robust solutions to the problem for charged electrode surfaces.[60,68,92,93]

In addition to the electrostatic interactions, non-electrostatic terms are required to precisely define solvation interactions. Traditionally, these terms are split into the cavitation energy associated with the formation of the cavity in the embedding system to host the solute and the repulsive and dispersion energies due to the Pauli electronic repulsion and electronic dispersion due to the non-local correlation effects [Eq. (15)].[94,95]

Using a compact formulation, the SCCS[59] and SSCS[56] models handle these non-electrostatic terms in terms of two functionals that are proportional to the quantum-surface and quantum-volume of the system,[96]

$$\Delta G_{sol} = \Delta G_{el} + \Delta G_{cav} + \Delta G_{rep} + \Delta G_{dis} \quad (15)$$

$$= \Delta G_{el} + (\alpha + \gamma) S_q + \beta V_q. \quad (16)$$

Alternatively, the empirical approach of Grimme to van der Waals interactions was also extended to model system-continuum interactions.[54] However, for slab interfaces, the non-electrostatic terms are usually regarded as less important, with reaction energies being mostly affected by the electrostatic terms (ΔG_{el}).[38,69] Moreover, the intensity of these interactions, controlled by the α, β, and γ parameters, is usually tuned so as to reproduce experimental results, usually related to the solvation free energy of small organic molecules in specific solvents. However, in the calculation of free energies for materials surfaces under electrochemical conditions, non-electrostatic terms are most often neglected due to their associated parameterization and less general definitions. The non-electrostatic terms are used as fitting parameters for determining the accurate solvation energies of zero-dimensional solutes. While adding the volume term allows us to improve the accuracy in the solvation energies of small isolated systems, its meaning and use is less evident for most materials simulations. The reason for this is the fact that most materials simulations adopt the slab approximation for studying the surface of a semi-infinite system. The solvation energy of such an approximate model should not depend on the number of layers considered, which instead affect the quantum volume of the system. Moreover, also for materials that are a few atoms thick and do not involve the slab approximation, as in case of the two-dimensional systems, the inclusion of non-electrostatic terms will only result in uniform energy shifts since the quantum-mechanical cavities change marginally.[38,69]

V. COMPUTATIONAL HYDROGEN ELECTRODE (CHE) METHOD

The CHE approach, pioneered by Nørskov and co-workers, presents a promising way of modeling the reaction thermodynamics at the electrochemical interfaces.[37] It was introduced to study the electrosorption free energy of O_2 reduction reaction in fuel cells. At a later stage, this method found to be efficiently useful for probing the reaction thermodynamics of many other electrochemical reactions. It takes an approximation of concerted electron and proton transfer in every electrochemical step. We discuss this approach here in light of one of the O_2 reduction reaction (ORR) steps. Let us consider the reaction step shown in Eq. (17). The adsorbed state of the intermediate on the electrode surface is denoted by OOH^*, and * denotes the reactive center,

$$* + O_2 + H^+ + e^- \rightarrow {}^*OOH. \tag{17}$$

The reaction free energy for this step will be

$$\Delta G = \Delta E + \Delta ZPE - T\Delta S - (\mu_{H^+} + \mu_{e^-}). \tag{18}$$

Here, ΔE, ΔZPE, and $T\Delta S$ denote the DFT calculated formation energy, zero-point energy, and entropic correction terms, respectively, for OOH^* from O_2.[16,97,98] Estimating the chemical potentials of the H^+ and e^-, μ_H^+ and μ_e^- poses the greatest challenge.

Within the CHE approximation, these chemical potential values are calculated with respect to reversible hydrogen electrode (RHE) as the reference electrode. At an applied zero potential and 1 bar pressure, H^+, e^-, and gaseous H_2 will maintain an equilibrium within the RHE. Therefore, the values for this reference electrode ($\mu_{H^+}^{ref}$ and $\mu_{e^-}^{ref}$) would be

$$\mu_{H^+}^{ref} + \mu_{e^-}^{ref} = \mu_{H_2}/2. \tag{19}$$

At an applied potential ϕ_{RHE}, the chemical potential will be lowered. The difference in the chemical potential at the applied potential and the reference value ($\mu_{H^+}^{ref}$ and $\mu_{e^-}^{ref}$) will be equivalent to the applied potential,

$$\phi_{RHE} = -(\mu_{e^-} - \mu_{e^-}^{ref})/e. \tag{20}$$

Here, e is the elementary electronic charge. Using Eqs. (19) and (20), a general expression for μ_e^- in Eq. (18) is obtained as

$$\Delta G = \Delta E + \Delta ZPE - T\Delta S - (\mu_{H_2}/2 + e\phi_{RHE}). \tag{21}$$

In Fig. 4(b), the free energy diagram calculated using the CHE approach for the ORR pathway on the Pt(111) surface is shown. Without any applied potential, the reaction steps are exothermic; however, at the O_2 reduction equilibrium potential (1.23 V), some of the reaction steps become uphill in energy. The OH^* to H_2O step shows to be the potential determining step. The maximum potential at which all the reaction steps remain exothermic is 0.75 V and should be denoted as the limiting potential. This value agrees well with the experimental findings.[99,100]

VI. BEYOND THE COMPUTATIONAL HYDROGEN ELECTRODE

The CHE method enabled detailed studies of the electrochemical reaction pathways and high-throughput screening of material databases for electrocatalysis.[18,24,29] The simplistic approach and computational efficiency of this model gave access to analyze the surface Pourbaix stability of the materials and aqueous degradation pathways under varied electrochemical conditions.[99,101–104] However, there are several limitations associated with the CHE method. First, in this model, the kinetic barriers for the proton-coupled electron transfer steps are not addressed appropriately.[105–107] A surmountable kinetic barrier under the applied limiting potential is one of the major assumptions in this model. This brings in the conceptual equivalence between the thermodynamic-limiting step (or potential limiting step under an applied bias) and the rate-limiting step for all the reaction pathways. Second, decoupled proton and electron transfer mechanisms could not be effectively probed using the CHE approach.[107,108]

Third, the free energy for electrosorption under an applied bias would be effectively estimated from CHE method when the interfacial electric field interactions have minimal effect on the binding energies of the intermediates.[29] The polar intermediates, e.g., adsorbed oxygenated species or CO_2, show considerably higher surface–adsorbate dipole field interactions. It has been seen that the interfacial electric field due to electrode surface charge and the ionic electrolyte ions tune both the binding energies and adsorption configurations of the intermediates involving these adsorbates.

In an electrochemical setup, a charged electrode attracts electrolyte counter ions from the solution. Several models have been proposed to define the structure of the electrode/electrolyte interface. A statistical distribution of the electrolyte ions at

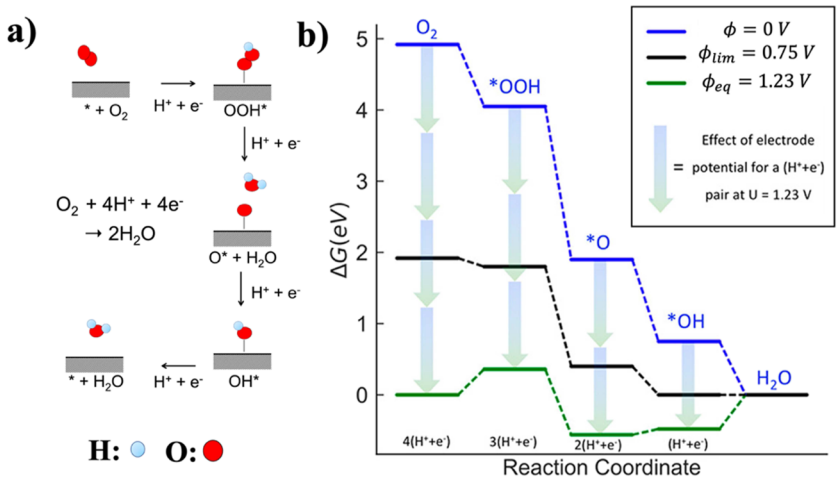

FIG. 4. (a) The 4-step proton-coupled electron transfer (PCET) steps for the O_2 reduction reaction (ORR) proposed under the CHE framework.[37] The blue and red spheres denote the H and O atoms. (b) Free energy diagram for ORR on the Pt (111) surface at different applied electrode potentials, reproduced with permission from Kulkarni *et al.*, Chem. Rev. **118**, 2302–2312 (2018). Copyright 2018 American Chemical Society. The blue lines are obtained at the 0 potential, the green lines at 1.23 V, and the black line at the limiting potential of 0.75 V.

the charged electrode/electrolyte interface, illustrated by the Gouy–Chapmann–Stern (GCS) model, has been found to be most precise so far.[109,110] This model predicts the formation of a double-layer structure composed of a compact and diffuse layer by the electrolyte ions at the electrode/electrolyte interface [Fig. 5(a)]. The excess electrons on the electrode surface generate a surface dipole, which results in the formation of a compact layer of counter-charged electrolyte ions near the electrode surface. This compact layer is termed the inner Helmholtz layer. Further away from the electrode surface, a diffused arrangement of the electrolyte ions is seen. Figure 5(a) shows a schematic arrangement of the electric double layer for a negatively charged electrode surface. An interfacial electrostatic potential [as denoted by the red dotted line in Fig. 5(a)] is formed due to the double-layer arrangement of the electrolyte ions.

To incorporate the effect of the interfacial electric field at the electrode/electrolyte interfaces while performing the binding energy calculations of the intermediates in an electrochemical reaction pathway, several corrections are added to CHE method. In Secs. VI A and VI B, we discuss a few of these simulation methods.

A. Cell and charge extrapolation methods

The cell extrapolation method is proposed by Nørskov and co-workers to model the electric field effects at the wet-electrified interfaces in the presence of an explicit water-bilayer.[27,111] In this model, the potential of the electrode surface is modulated by varying the coverage of dissolved H^+ ions in the explicit bilayer of water on top of the electrode surface. It is assumed that hydrogen atoms get solvated and form a pair of electron and proton. The proton is stabilized by the water molecules in the water bilayer, whereas the electron moves to the material interfaces and varies its surface charge density and work function. The electrode potential (U) could be obtained by Eq. (22) from the work function of the electrode, ϕ, with reference to the normal hydrogen electrode (NHE), ϕ_{NHE},[112,113]

$$U = \phi - \phi_{NHE}. \tag{22}$$

In a calculation setup with finite cell size, the proton concentration in the water bilayer will change for an initial and final state for a proton-coupled electron transfer reaction.[111] This results in an alteration of the electrode work function or the electrode potential during the reaction. To remove this finite cell-size error and achieve a constant potential simulation setup, DFT calculations should be performed with an infinitely large unit cell. With the increase in the cell-size, the change in surface charge density during the electron or proton transfer from initial to transition state to final state will be minimal. However, with bigger cell-size and large number of atoms, the computational cost will be very high as the DFT calculations scale as $O(N_e^3)$, with N_e being the number of electrons in the simulation setup. Skúlason *et al.* suggested an extrapolation scheme to overcome this issue.[111] In this scheme, the calculations are performed with varying cell sizes by keeping the proton coverage (or electrode potential) constant on the explicit water bilayer. Plotting the activation and reaction-free energies as a function of the change of potential (ΔU) between the initial and final states for different unit-cell sizes shows a linear dependence. Extrapolation of the best-fitted line to a zero ΔU limit will therefore correspond to the activation and reaction free energy values at infinite cell size for the corresponding proton coverage or applied potential. Figure 5(c) shows the simulation setup and reaction free energy plot for the cell extrapolation scheme used to determine the activation barrier and reaction free energy values of the Volmer step of the HER.

While the cell extrapolation method could efficiently be used to model the reaction energetics for different electrochemical reactions, the repeated computations with varying cell sizes possess a great extent of computational complications for multi-step reaction

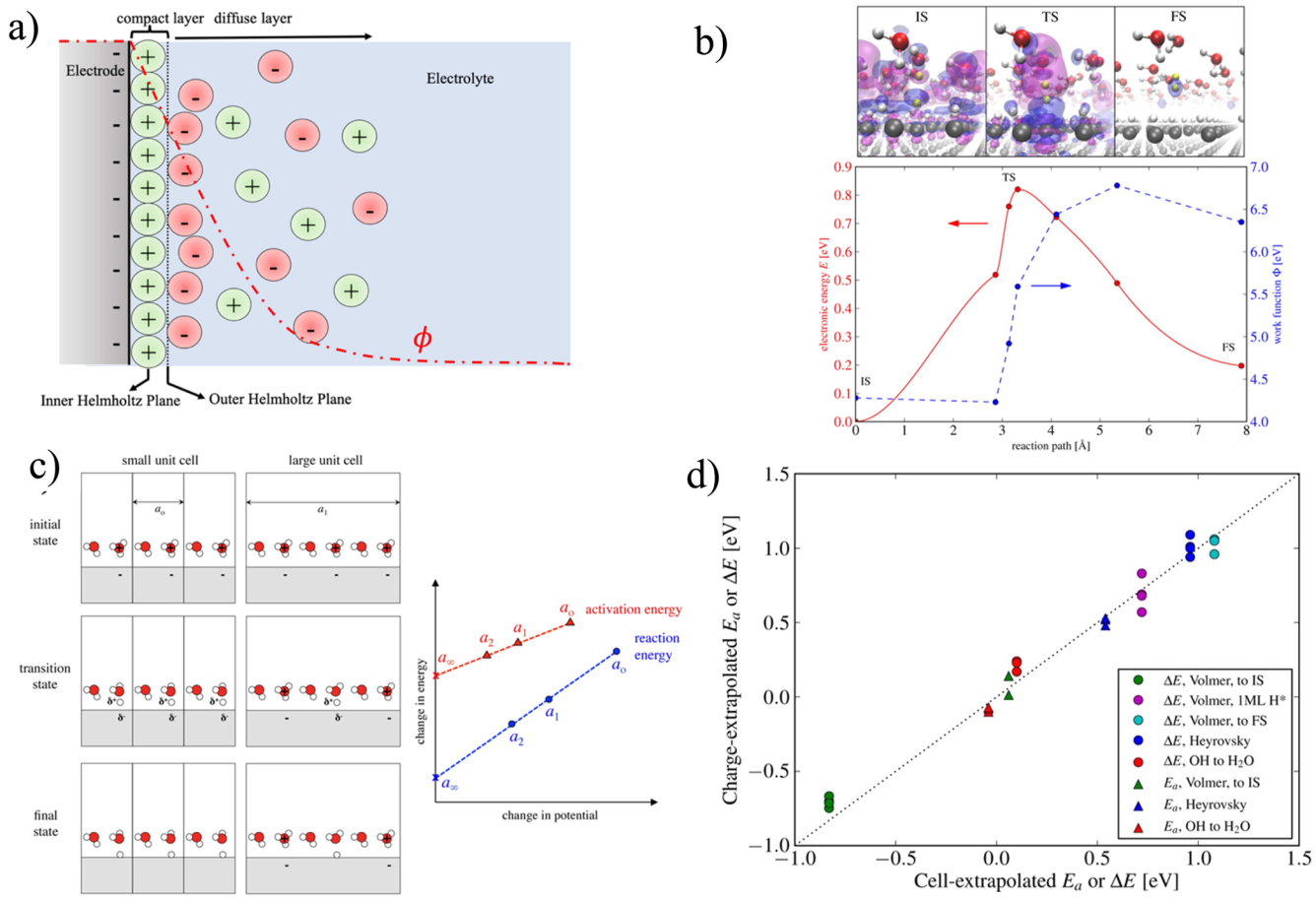

FIG. 5. (a) Schematic representation of the electrochemical interface for a negatively charged electrode surface. The green and red spheres represent the positively and negatively charged electrolyte ions, respectively. The red dotted line is electrostatic potential distribution, ϕ, as a function of the distance from the electrode surface. (b) The transition state of the Heyrovsky reaction on a 3 × 4 Pt(111) surface with adsorbed proton atoms. The charge density difference isosurfaces of the initial, transition (TS), and final states are shown in the top panel, whereas the electronic energy in eV (red solid line) and corresponding work function in eV (blue dotted line) for the reaction path are shown in the bottom panel (c) The cell-extrapolation method for determining the reaction energetics and activation barrier (in blue and red, respectively) for a proton transfer reaction on the metal surface. The different cell sizes are denoted by a_0, a_1, and a_2. a_∞ corresponds to the extrapolated infinite cell size. (d) Comparison of the reaction energetics for HER calculated using the cell-extrapolation and charge-extrapolation methods. Further details are given in the inset of figure. The figures are reproduced with permission from Chan and Nørskov, J. Phys. Chem. Lett. **6**, 2663–2668 (2015). Copyright 2015 American Chemical Society.

processes. Therefore, a computationally more effective method is proposed later by Chan and Nørskov to address this issue. In the revised scheme, the surface charge of the electrode is extrapolated and involves a limited number of DFT simulations.[114]

The charge extrapolation method is based upon the charge partitioning scheme, where electrosorption free energy could be expressed as the sum of chemical (E_{chem}) and electrostatic (E_{el}) terms as follows:

$$E = E_{chem} + E_{el}. \tag{23}$$

Following a similar setup as the cell extrapolation method, the chemical contribution could be obtained from DFT calculations of the reaction energetics. On the other hand, the electrostatic term is determined following a simple capacitive model, where E_{el} would be expressed using the surface charge ($\theta \approx q/N$) and capacitance (C) of the electrode with N atoms by $(e\theta)^2/2C$. The total reaction free energy at a constant potential (ϕ_1) between initial and final states (1 and 2) would be obtained using

$$E_2(\phi_1) - E_1(\phi_1) = [E_2(\phi_2) - E_1(\phi_1)] + \frac{(q_2 - q_1)(\phi_2 - \phi_1)}{2}. \tag{24}$$

Here, $E_1(\phi_1)$ and $E_2(\phi_2)$ correspond to the DFT calculated free energies of the initial and final states, where the variation in proton coverage results in modulation of the electrode potential ϕ_1 and ϕ_2 between the initial and final states. The charge difference between the initial and final states (q_2–q_1) due to the variation of proton numbers could be obtained from Bader analysis. For an elementary step reaction, such as HER, the reaction free energies and

activation barrier values calculated with this scheme show a reasonable agreement with values obtained from the cell extrapolation method [Fig. 5(d)]. However, for complex electrochemical reactions, the results could be very sensitive to the simulation parameters, particularly related to the charge partitioning scheme. Furthermore, the specific arrangement of the water structure could imply additional surface-dipole moments. This will affect the charge partitioning method and therefore would lead to unphysical tuning of the work-function.

B. Grand canonical potential simulations

The grand canonical potential simulations give access to the thermodynamic variables relevant to define an experimental electrochemical setup by the Legendre transformation of the DFT calculated free energies. Several approaches have been developed in the literature to perform the grand canonical simulations of electrified interfaces.[38,39,41,115–117] In these approaches, to define the thermodynamic potential of the electrochemical interface, the surface charge or the work-function of the electrode is used as the descriptor. Here, we give a brief overview of two simulation techniques for the grand canonical potential method, where direct control of the electrode potential is achieved using a charging scheme and the work function scheme.

Using the work function (ϕ) of the electrode as the driving force, the grand potential free energy $J(\phi, \mu_a)$ of an electrochemical simulation setup comprising an electrode slab with N_s atoms, absolute surface charge N_e^{abs}, and N_a adsorbed ions on the surface is described by

$$J(\phi, \mu_a) = \min_{(N_e, N_a)} J_{IP}(N_s, N_e, N_a). \tag{25}$$

In Eq. (25), $J_{IP}(N_s, N_e, N_a)$ is the interfacial free energy of the electrochemical interface, which is determined by the Legendre transformation of the DFT calculated free energy $G_{DFT}(N_s, N_e, N_a)$ using

$$J_{IP}(N_s, N_e, N_a) = G_{DFT}(N_s, N_e, N_a) - \sum_{N_s} \mu_s N_s - \sum_{N_a} \mu_a N_a + e\phi N_e^{abs}. \tag{26}$$

The absolute surface charge N_e^{abs} corresponds to an electronic charge of the electrode slab due to the exchange of electrons with the external circuit, as denoted by Eq. (27). $\frac{q_a}{e} N_a$ is the amount of charge compensated due to the adsorption of the intermediates with $\frac{q_a}{e}$ charges, whereas N_e^{net} denotes the excess surface charge on the electrode, which attracts counter ions of the electrolyte in the diffused layer,

$$N_e = \frac{q_a}{e} N_a + N_e^{net}. \tag{27}$$

μ_a in Eq. (26) is the electrochemical potential of adsorbate ions and μ_s is the chemical potential of the slab atoms. In general, $N_s \mu_s$ refers to the free energy of bulk crystals, which serves as the atomic reservoirs for the formation of electrode slab.

The reaction free energy ΔG_{ads} for the adsorption of ionic intermediates is determined from the grand canonical free energies of the electrode slab with and without ionic adsorbates, as shown in Eq. (6).[38,69] The interfacial free energy of the clean electrode slab upon interpolation on the electrode potential (ϕ) followed by the minimization with respect to the electronic charges (N_e) provides the grand potential free energy $J(\phi)$ of the electrode slab without the adsorbates. On the other hand, for the electrode surface with a varying surface coverage of adsorbates, the interpolation and minimization are performed against both the surface charges and adsorbate coverage to calculate $J(\Phi, \mu_a)$,

$$\Delta G_{ads}(\Phi, pH) = J(\Phi, \mu_a) - J(\phi). \tag{28}$$

The ionic electrochemical potential μ_a could be determined by combining the DFT calculated free energies of the involved species with an experimental value. For example, the electrochemical potential for a proton in an aqueous medium could be defined by the standard hydrogen electrode (SHE @ 4.44 V), as shown in Eq. (29). In the aqueous medium, the proton is considered to be in equilibrium with the gaseous H_2 molecule ($H^+ \leftrightarrow \frac{1}{2} H_2$),

$$\mu_H = \frac{1}{2} \mu_{H_2(g)} - k_B T \ln(10) \cdot pH + 4.44 \text{ eV}. \tag{29}$$

The chemical potential μ_{H_2} for gaseous H_2 is determined by DFT calculation, and pH corresponds to the proton concentration of the aqueous medium. Now, for a charge neutral system ($N_e^{net} = 0$), substituting the value for μ_H [Eq. (29)] in the interfacial free energy expression in Eq. (25) and equating N_H to 1, a similar expression is obtained as shown earlier for CHE formulation in Sec. IV,

$$J(\phi, \mu_H)^{CHE} = G^{DFT}(N_s, N_e, N_H)) - G_{bulk} - \left[\frac{1}{2} \mu_{H_2(g)} - k_B T \ln(10) \cdot pH + 4.44 \text{ eV}\right]. \tag{30}$$

The simulations are performed at varying charge setups of the electrode slab to interpolate the interfacial free energy values on electrode potential ranges. Therefore, the accuracy of the calculated grand potential free energies largely depends on the continuum electrolyte definitions. Furthermore, a symmetric slab setup is essential to reduce the potential error on the electrode work function due to the asymmetric charge distribution of the electrolyte diffused layers.

Another point to be noted is the calculation of the forces within the grand canonical ensemble under the constant-potential scheme. In the atomistic simulations, the forces are important to search for the stationary points. The minimization scheme discussed above for the constant-potential calculations are based upon the forces calculated as the negative gradient of the potential energy surface (PES). However, in computational electrochemical setups, the grand canonical potential free energy surface is critically more important as the electron number (N_e) is the free variable controlling the electronic chemical potential. Therefore, forces calculated by the negative gradient of the grand canonical potential energy rather than PES would be more appropriate for structure minimization, saddle point calculations, or molecular dynamics simulations under constant-potential electrochemical setups.

To illustrate the importance of grand canonical potential energy surfaces for electrochemical calculations and relevance with PES, in a recent study, Peterson and co-workers compared the results of constant-charge and constant-potential DFT simulations

on the H-adsorbed Pt surface.[118] It is observed that analytical derivatives at any point on both the potential energy surfaces are equivalent. Hence, stationary point searches based on forces calculated using both these methods would be equivalent. While the equivalence of both the methods is evident from this study; however, to draw a general conclusion on this and test the validity for other surfaces, further studies are indeed needed.

Alternatively, using the surface charges as a descriptor instead of the work function could reduce the dependence on the continuum electrolyte parameters. The DFT calculated energy for a charged electrode slab could be expressed by a Taylor expansion of the electronic energy of the neutral slab $[E^{DFT}(N_e^{net}=0)]$ with respect to the net electronic charge N_e^{net} as follows:[41,115]

$$E^{DFT}(N_e^{abs}) = E^{DFT}(N_e^{net}=0) + \underbrace{\frac{\partial E^{DFT}}{\partial N_e^{net}}}_{-e\phi_0}\Bigg|_{N_e^{net}=0} N_e^{net} + \frac{1}{2}\underbrace{\frac{\partial^2 E^{DFT}}{\partial^2 N_e^{net}}}_{\frac{e^2}{C}}\Bigg|_{N_e^{net}=0} (N_e^{net})^2. \quad (31)$$

Here, C is capacitance and ϕ_0 is the potential of zero charge (pzc) for the neutral slab. With the addition of zero-point energy correction and entropic corrections to Eq. (31), the resulting energy equation will be similar to the interface free energy, as shown in Eq. (26). The reaction free energy value could be expressed as

$$\Delta G = \Delta G^{DFT}(N_e^{net}=0) + e(N_{e,2}^{net} - N_{e,1}^{net}) \times \left[\frac{e(\overline{q_a N_a} + N_e^{abs})}{C} - \phi_0\right]. \quad (32)$$

$\overline{q_a N_a}$ is the averaged explicit charge due to the adsorbed ionic intermediates of the initial and final states. This is denoted as $\frac{q_{a,2}N_{a,2}+q_{a,1}N_{a,1}}{2}$. N_e^{abs} is obtained from the implicit charge as imposed during the simulation. With this expression for the grand potential free energy, the dependence on the work function of the electrode potential is removed. However, the quantitative evaluation of the term $(N_{e,2}^{net} - N_{e,1}^{net})$ enhances the computational cost of the simulation method. The net absolute charge between the two surface states could be obtained following the cell extrapolation method. For an electrochemical simulation involving minimal charge transfer between the initial and final states, the contribution from the term $(N_{e,2}^{net} - N_{e,1}^{net})$ would be minimum and hence neglected. However, this term could be significant for several electrochemical reactions and will bring in computational complexities.

VII. KINETICS OF ELECTROCATALYTIC REACTIONS: BEYOND THE THERMODYNAMIC OVERPOTENTIALS

The understanding of the multi-step electrochemical reactions most often relies on the thermodynamic data, where the reaction free energies of the intermediates are used to predict the performance of the electrocatalysts. The underlying kinetics related to reaction free energy barriers are neglected due to computational challenges in calculating these energy values.[29] The Sabatier principle establishes a general connection between the thermodynamics and the kinetics of the reaction processes.[119,120] According to this principle, the reaction intermediates should be optimally bound to the reactive sites for an active catalyst. With this principle, in addition to the Brønsted–Evans–Polanyi (BEP) relations, it is assumed that the activation barrier scales linearly with the thermodynamics, leading to a smaller kinetic barrier at an applied potential.[121] Therefore, the scaling relations of the intermediate binding energies as derived from the thermodynamic data would preferably predict the activity of the electrocatalysts and allow to plot a reactivity volcano to define their performance.[120]

However, the thermodynamic overpotential η_{TD} derived at zero applied potential depending upon an elementary step with the highest reaction free energy (potential determining step, pds) might not favorably predict the rate-limiting step for all reaction pathways. In general, for a multi-step reaction pathway, the rate-determining step (rds) might involve more than one elementary reaction step, including all the intermediates preceding the rds.[122] A comparison of the thermodynamic and kinetic data are needed to predict the general activity of the electrocatalysts.

Analyzing the rate-limiting steps and thermodynamic data on a comprehensive set of electrocatalysts for oxygen evolution reaction, Over and Exner introduced a potential dependent activity descriptor to define the performance of the electrocatalysts. This descriptor is denoted as $G_{max}(\eta)$, which gives a qualitative understanding of both the pds and rds for a multi-step electrochemical reaction pathway.[121–123]

$G_{max}(\eta)$ is determined from the sum of the reaction free energy values defining the transition from step with the lowest to the highest free energy at an applied overpotential η. For the case with rds = pds, both the thermodynamic overpotential and the $G_{max}(\eta)$ are found to be good descriptors for defining the activity of the electrocatalyst. However, for pds ≠ rds, at an applied overpotential, the reaction free energies are shifted, resulting in a renumbering of the reaction steps to account for the optimization of the reaction energy profile. Figure 6 shows the OER free energy diagram. The reaction pathway in Fig. 6(a) shows that at zero overpotential, pds step corresponds to step (ii) → (iii), while based upon $G_{max}(\eta)$, the rds corresponds to the reaction step (i) → (iii). The TS No. 3 has the highest activation energy. At an applied overpotential η = 0.3 V, the reaction free energies are shifted. On renumbering the reaction steps at η = 0.3 V, $G_{max}(\eta)$ approaches $G_{rds}^{\#}$.

Screening of a comprehensive set of materials for electrocatalyzing OER based upon $G_{max}(\eta)$ values shows a volcano relation represented in Fig. 6(c), as, in general, observed using η_{TD} as the descriptor. However, there is a qualitative difference with respect to materials' activity with these two descriptors. A correlation between $G_{max}(\eta)$ and η_{TD} for these same set of materials does not show a linear scaling as plotted in Fig. 6(d). At lower thermodynamic overpotentials, for most of the data points, a strong correlation is observed. However, a considerable deviation from the linear best-fit line at higher overpotential values is observed. Therefore, screening studies involving both $G_{max}(\eta)$ and η_{TD} as descriptors to qualitatively define the activity of the electrocatalysts might be more

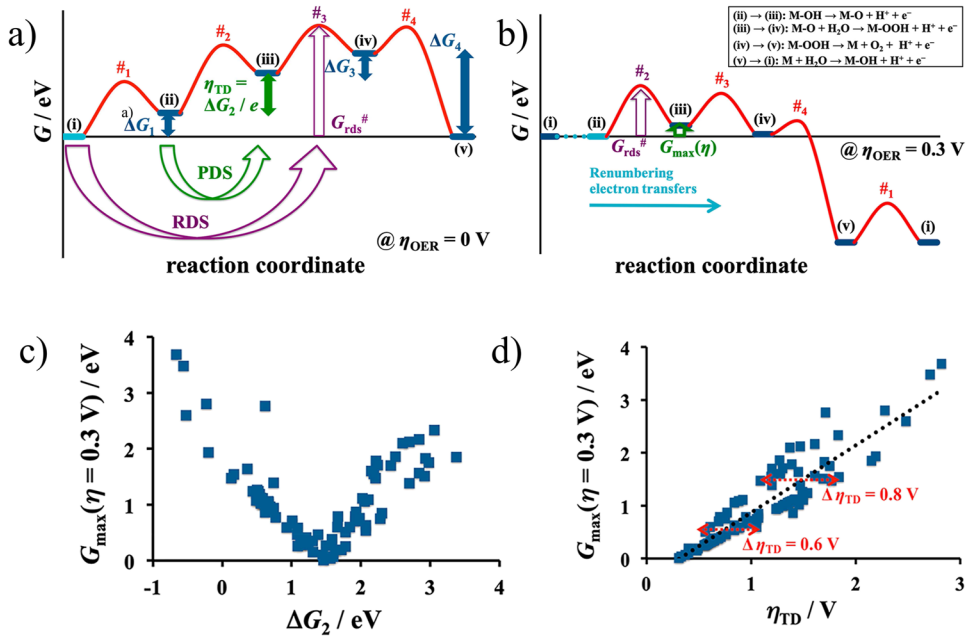

FIG. 6. The potential energy diagram for the OER mechanism and the concept of the thermodynamic overpotential (η) are addressed. In the free-energy diagram, η_{TD} refers to the potential-determining step (pds), whereas rds refers to the rate-determining step. (b) Renumbering of the electron-transfer steps in the presence of an applied electrode potential. Using this idea, η_{TD} approaches $G^{\#}_{rds}$. (c) Activity volcano plot using $G_{max}(\eta = 0.3\ V)$ as the descriptors for OER. Different types of materials, such as transition-metal oxides, porphyrins, perovskites, metal oxides, and functionalized graphitic materials, are taken into account. (d) A comparison of $G_{max}(\eta = 0.3\ V)$ vs η_{TD} as the activity descriptors. At lower η_{TD}, both the descriptors would give similar results; however, the results would differ at high η_{TD} values. The figures are reproduced with permission from Exner, ACS Catal. **10**, 12607–12617 (2020). Copyright 2020 American Chemical Society.

appropriate. η_{TD} allows identifying the pds, whereas $G_{max}(\eta)$ would allow identifying the rds.[74,122]

VIII. MICROKINETIC MODELING OF REACTION PATHWAYS

Micro-kinetic modeling is a well-known technique that is used to correlate the atomic or elementary reaction description to the experimental rate of reaction pathways. However, on the catalyst surface, the reaction rate is influenced by several factors, such as the structural, electronic, reaction thermodynamics, and activation barrier.[25] Therefore, due to the high dimensionality of the problem, the complete solution of the reaction rate on the catalyst surface is very expensive.

In recent years, comprehensive analysis of reaction energetics on several catalyst surfaces has shown a correlation between the binding energies of the intermediates and the transition barrier, which has reduced the dimensionality of the parameter space required for defining the reaction kinetics.[124–127] These descriptor-based approaches, denoted as the micro-kinetic modeling of reaction pathways, have reduced the complexity of the problem and enabled rational modeling of the reaction kinetics based upon the thermodynamic data.

The thermodynamic energies of the reactants, intermediates, and products form the central inputs to the microkinetic modeling. For a simple reaction,

$$aA + bB \rightarrow cP + dD. \tag{33}$$

The rate of the reaction (r) is expressed using the rate constant (k), reactant concentration ([A] and [B]), and the stoichiometric coefficient as

$$r = k[A]^a[B]^b, \tag{34}$$

$$k = A * e^{\frac{-\Delta G_a}{k_B T}}. \tag{35}$$

Here, A is the pre-exponential factor, ΔG_a is the reaction activation barrier, k_B is the Boltzmann constant, and T is the temperature.

For a multi-step reaction process, defining the rate of the reaction would involve analyzing the rate of the intermediate steps. To reduce the computational complexities, a few assumptions denoted as the mean-field approximations are taken into account.[25,128–130]

In the mean-field modeling, the surface sites and the surface species are assumed to be uniformly distributed, and the rate is assumed to depend upon the average coverage of the reactant species.[131] Therefore, for a multi-step reaction involving several elementary steps, the rate will be given by

$$r = k_+ \Pi\theta_{react}\, p_{react} - k_- \Pi\theta_{prod}\, p_{prod}. \tag{36}$$

In this equation, + and − signs denote the forward and backward reaction steps. The rate constants k_+ and k_- are defined by

$k_+ = A * e^{\frac{-\Delta G_{a+}}{RT}}$ and $k_- = A * e^{\frac{-\Delta G_{a-}}{RT}}$, respectively, where ΔG_{a+} and ΔG_{a-} are the activation barriers for the forward and the backward reaction process. Using the transition state theory (TST), the pre-exponential factor A becomes $\frac{k_B T}{h}$ (here, h is the Planck constant) and $\Delta G = \Delta H - T\Delta S$.

Multi-precision root finding algorithms are used to determine the rate of the reaction steps and coverage of the intermediates. The rate equations are solved based upon the steady state approximation of the intermediates, giving $\frac{d\theta_i^{int}}{dt} = 0$. With the site conservation constraint, therefore the coverage of the reaction intermediates will be $\sum \theta_i^{int} = 1$.

The reaction energy barriers (ΔG_a) are calculated as $\Delta G = \Delta H_a - T\Delta S$. ΔH and ΔS values are the activation barriers and entropic factors that could be determined using the DFT calculations.[97] However, for large reaction networks, ΔH calculations become very challenging, and therefore, the Brønsted–Evans–Polanyi (BEP) relationships are used.[132,133] According to BEP relationships, activation energies could be expressed as the linear function of the heat of the reaction (Fig. 7) as[124,134]

$$\Delta H_a = \alpha \Delta H_{rxc} + \beta, \tag{37}$$

where α is the proximity factor taken as a value between 0 and 1 and the intercept β is the intrinsic activation barrier.

In a few recent studies, it has been observed that α and β are independent of catalyst material, and the variations in rate constants could be described by the variations in the reversible potentials for the different reaction steps.[135–137] For water oxidation and O_2 reduction reactions, $\alpha = 0.5$ and $\beta = 0.26$ eV have been found to precisely define the reversible current density on the metal surfaces with great accuracy as in the experiments. However, the explicit solvent interactions could affect these values.[138,139] The estimation of these values could allow more accurate estimation of the reaction rates and catalytic activity.

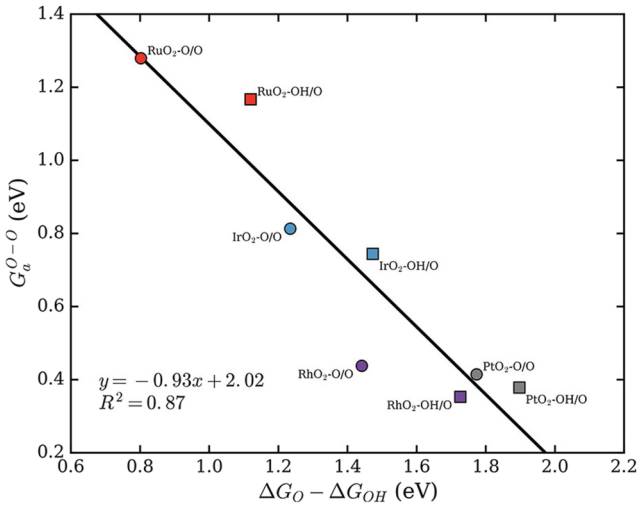

FIG. 7. The scaling relationship between the O–O coupling activation barrier for the various transition metal rutile (110) surfaces calculated at different surface coverages of OH and O adsorbates with respect to $\Delta G_O - \Delta G_{OH}$. Reprinted with permission from, Rankin and Greeley, ACS Catal. **2**, 2664–2672 (2012). Copyright 2012 American Chemical Society.

Using the rate of the reactions, the turnover frequency (TOF) values could be determined to denote the activity of the catalysts.[131] TOF is defined as the rate of the reactions computed per active site of the catalyst.

While optimal binding of the reaction intermediates are referred to have greater catalytic activity conventionally, in a recent experimental study, the kinetic parameters are found to play critical roles in determining the reaction rates. Schlögl and co-workers conducted an investigation of 14 *d*-metals and two *sp*-metal catalysts for H_2 evolution reaction activity.[140] The catalytic activity of the noble metal surfaces show a strong dependence on the kinetic parameter, such as the pre-exponential frequency factor, in addition to the surface coverage of protons and reaction energetics. Studies are still ongoing to accurately estimate the different factors influencing the reaction kinetics. The complexities associated with the estimation of electrochemical barriers have been one of the major reasons limiting the accurate definitions of these parameters.

IX. THERMODYNAMIC EVALUATION OF ELECTROCHEMICAL STABILITY AND CORROSION OF MATERIALS

In addition to the lower thermodynamic overpotentials and higher turnover frequencies, the catalytic performance of the electrocatalysts is influenced by the electrochemical stability against aqueous degradation.[141] Several efforts have been devoted in the past to characterize the materials' stability under varied electrochemical conditions.

Analyzing the experimental thermodynamic data for reactions involving the pure elemental forms, aqueous ions, and oxides in the aqueous phase, Marcel Pourbaix established the first electrochemical phase diagrams for a set of 85 elements in the Periodic Table.[142–144] These phase diagrams are denoted as the Pourbaix diagram and form an accessible tool to understand the corrosion profile and electrochemical stability of the elemental solids under an applied potential and solvent pH. However, for binary and multi-component systems, following a similar method, the formulation of aqueous phase diagrams possesses an enormous challenge. The lack of complete knowledge of the composition space resulted from the experimental characterization of thermodynamic data for the involved multiple aqueous ions and degradation products, a formidable task.

To enable a comprehensive analysis of aqueous products for a larger set of compounds with different compositions, in recent years, DFT simulations have been designed to capture the electrochemical stability of materials. In this section, we discuss a formalism for the prediction of solid-aqueous equilibrium by combining first-principles calculations with experimental aqueous states.

Following the CHE approach, a computationally rigorous method has been proposed by Persson *et al.*,[101] which led to analyzing the electrochemical degradation free energy values of solids at various electrochemical conditions. In this scheme, for mapping the aqueous phase diagram, the standard state reaction Gibbs free energy of the redox reactions in an aqueous medium are determined using the DFT calculations. For example, the Gibbs free energy for each species resulting from the aqueous phase redox reactions of a

binary system (M-X) at an applied potential and solvent pH is given by

$$\Delta G_i(c_i, pH, \phi) = \Delta G^o + 0.059 * \log c_i - n_O \mu_{H_2O} + 0.059 * (n_H - 2n_O) * pH + (-n_H + 2n_O + q_i)\phi. \quad (38)$$

c_i is the concentration of the species, n_H and n_O are the number of H and O atoms, respectively, and μ_{H_2O} is the formation energy of water set to −2.46 eV. Here, q_i is the charge of the aqueous product, which could be positive, negative, or zero. The standard free energies (ΔG^o) for the elemental gaseous and solid compounds are determined from DFT. On the other hand, the reference energies for ionic species are obtained from the experimental free energy values of these species from the reported databases and experimental Pourbaix data repositories.[142–144] A correction scheme is introduced to reduce the inconsistencies between the calculated values and experimental data. For example, the free energy of an aqueous species is denoted by Eq. (39), where $\Delta G_i^{o,\exp}(aq)$ is the experimental value and ΔE_{corr} is energy correction,

$$\Delta G_i^o(aq) = \Delta G_i^{o,\exp}(aq) + \Delta E_{corr}. \quad (39)$$

The correction term refers to the Gibbs free energy difference between the experimental value and the DFT calculated reference solid. To clarify this, in Eq. (39), the correction term for $Li^+(aq)$ is shown. Li_2O is chosen as the representative reference for DFT calculations,

$$\Delta E_{corr}(Li^+(aq)) = \frac{1}{2}\left[\Delta G_{Li_2O}^{o,DFT} - 2\mu_{Li}^{ref} - \mu_O^{ref} - \mu_{Li_2O}^{o,\exp}\right]. \quad (40)$$

Here, $\Delta G_{Li_2O}^{o,DFT}$ and $\mu_{Li_2O}^{o,\exp}$ are the DFT calculated Gibbs free energy and experimental formation energies of Li_2O, respectively. The reference chemical potential μ_{Li}^{ref} and μ_O^{ref} are determined from the DFT calculated free energy of elemental Li and molecular gaseous O_2. The standard free energy of multicomponent crystalline solids is also obtained following a similar scheme, where the correction term is added to the DFT calculated formation energy of the crystalline solid.

The Pourbaix diagram of the well-known elemental solids reported earlier by Marcel Pourbaix using the experimental data shows a good agreement with the aqueous phases and stability obtained using this theoretical formalism. In Figs. 8(a) and 8(b), a comparative overview of the theoretical and experimental Pourbaix diagram of Mn is shown. Most of the aqueous states and solid phases in the theoretical Pourbaix diagram are found to be at appropriate conditions as the experimental diagram.

Later, this formalism is expanded to evaluate the relative free energy of metastable materials under varied pH, applied potential, temperature, and different aqueous species concentrations.[145] The developed method proved to be very efficient in predicting the electrochemical and photo-chemical stability of various bulk interfaces and 2D materials.[69,141] Fig. 8(c) shows the Pourbaix diagram of triclinic-$FeVO_4$ calculated using this formalism in Ref. 145 Furthermore, this approach paved the path toward determining the automated probing of surface Pourbaix diagrams for many-element systems.[146,147]

X. APPLICATIONS OF THERMODYNAMIC MODELS FOR SIMULATIONS IN ELECTROCATALYSIS

The thermodynamic and kinetic approaches described in Secs. V–VIII have been used to perform computational screening of electrocatalysts for several applications. In this section, we report two applications, where the grand canonical approach discussed above has been incorporated into the computational workflows to screen the two-dimensional (2D) materials for their water-splitting efficiency and CO_2 reduction activity.

In a recent study, initiating from the large databases of 2D-materials, favorable candidates are screened based on their thermodynamic stability, electrosorption free energies of the reaction intermediates, and electrochemical stability under the applied pH and the potential.[74] Figure 9 shows the computational workflows employed for identifying best 2D-electrode materials for HER, OER, and ORR. The grand canonical simulations are performed with the implicit solvent environment.

A five-step screening method has been employed to screen the favorable 2D materials for HER. The initial step, the pre-screening step, involves screening the materials' stability based on the dynamic stability and exfoliation energy from the bulk materials. In the following step, the electrosorption free energies of H^+ ions onto the materials' surfaces are calculated to determine the electrocatalytic efficiency for HER and the thermodynamic overpotential values. The final steps involve band-gap calculations and electrochemical stability under reduction potential and acidic pH. Starting from a set of 258 initial materials from the materials cloud database,[148] 21 monolayers are found to have HER overpotential lower than 0.5 V, among which the 8 materials with the molecular formula CoO_2, FeS, 2H–NbS_2, 1T-NbS_2, 2H–$NbSe_2$, 1T-$NbSe_2$, 1T-MoS_2, and 1T′-$MoTe_2$ are identified with higher electrochemical stability.

A similar screening workflow has been employed to screen 2D-transition metal dichalcogenides (TMDCs) to find good electrocatalysts for OER and ORR.[74] The activity calculations and electrochemical stabilities are determined under an acidic medium. Among more than two hundred TMDC materials proposed in the recent computational databases,[148,149] the screening study enabled identifying seven materials for OER, whereas for ORR, around twenty materials are found to be active and stable.

Similar computational studies are performed to define the activity of single and diatom catalysts for CO_2 to CO reduction reactions.[150] Employing the computational grand canonical simulations, the binding energies of CO_2^* and $COOH^*$ intermediates are calculated on supported single and double transition metal atoms on defected graphene surfaces. Using these binding energies as the descriptors, kinetic models are developed to construct activity volcano plots based on the microkinetic approach discussed in Sec. VIII. Comparing their activity with the noble metal (211) surfaces, several single and diatom catalysts are identified with comparable activity as bulk Ag and Au (211) surfaces, as shown in Fig. 10(b).

XI. SUMMARY AND FUTURE PERSPECTIVES

In the previous sections, several theoretical developments are discussed, which enabled us to understand the characteristics and properties of solid–liquid interfaces. Most of these theoretical tools

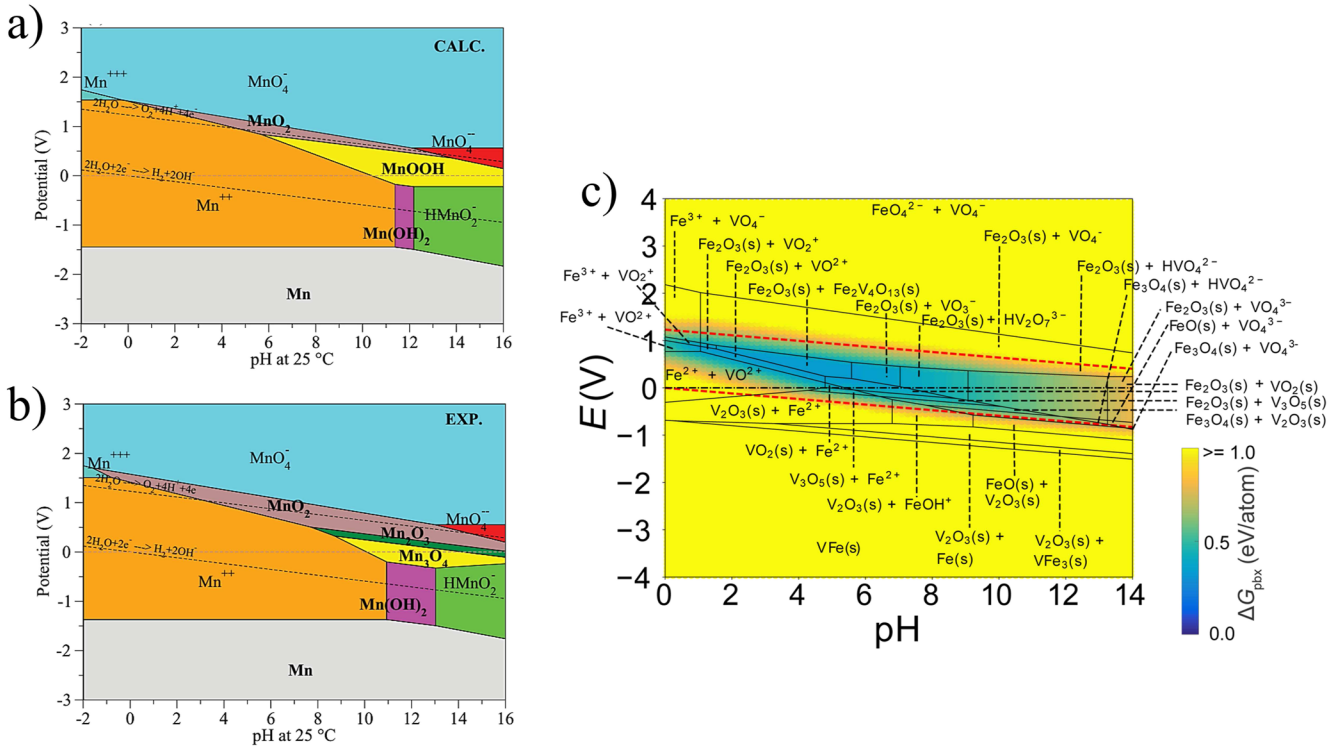

FIG. 8. (a) and (b) Mn Pourbaix diagrams at 25 °C with aqueous species at a concentration of 10^{-6} M. The diagram in (a) is obtained using the formalism developed by Persson *et al.*,[101] and (b) the experimental data from Ref. 142. (c) Fe–V–O–H metastable system Pourbaix diagram reported in Ref. 145. The color bar shows the free energy of dissolution, ΔG_{pbx}, of the metastable triclinic-$FeVO_4$ phase relative to the Pourbaix stable phases. Potentials of 0 V vs RHE and 1.23 V vs RHE are indicated by the red dashed lines. The respective aqueous and solid products are given in the figure. The figures (a) and (b) are reproduced with permission from Persson *et al.*, Phys. Rev. B **85**, 235438 (2012). Copyright 2012 American Physical Society, and figure (c) is reproduced with permission from Singh *et al.*, Chem. Mater. **29**, 10159–10167 (2017). Copyright 2012 American Chemical Society.

use the implicit solvent environment or reduced water configurations (while using hybrid explicit/implicit solvation). However, considering the real electrode–electrolyte interfaces, the operating environment is entirely different. *Ab initio* molecular dynamics simulations with a full explicit model for water molecules could enable studying these solid–liquid interfaces with great precision. Nevertheless, *ab initio* methods could be applicable only with a limited number of atoms.

In recent years, machine learning methods (ML) have been employed to probe the characteristics of these interfaces and their reactivity under various electrochemical reactions.[151–155] Various machine learning potentials have been developed to define the atomic interactions and electron densities for different solid–liquid interfaces, such as the metal/water and metal–oxide/water interfaces.[156–158] The machine learning potentials enable combining the principles from quantum mechanics with simple empirical atomic potentials to increase the accuracy of the simulation results.[159–162] With such setups, it has been possible to gain information about the geometry, electronic structure, and several properties of the solid/electrolyte interfaces, such as the polarizabilities,[163] electrostatic multipole moments,[164] atomic charges,[165–168] and electronic wavefunctions.[169] Furthermore, with the ML potentials, molecular dynamics simulations are performed with high accuracy as that of *ab* initio methods and as fast as that of classical force field methods.

Among a few of the ML models, kernel and artificial neural network (NN) based models are the ones found with most applications.[170,171] Kernel methods are computationally expensive, whereas in neural network methods, relatively greater size of the training data set is needed for benchmarking the models and improving their accuracy.

To mention a few, Behler–Parrinello Neural Network Potentials (NNPs) have been applied to simulate several electrochemical interfaces.[172] Mikkelsen and co-workers[173,174] took Pt metal (111)/water interface and created around 50000 structural databases [containing 32 water molecules on 3 × 4 Pt (111) slab] with different water arrangements to train the ML potentials for Pt metal (111)/water interfaces. MD simulations are then performed with these ML potentials, enabling the authors to characterize the water configurations at room temperature with accuracy as great as the AIMD simulation results. In another study, the high dimensional NNPs are used by Natarajan and Behler[175,176] to determine the structural properties and surface defect formations on the Cu/water interface. Performing MD simulations employing ML potentials with

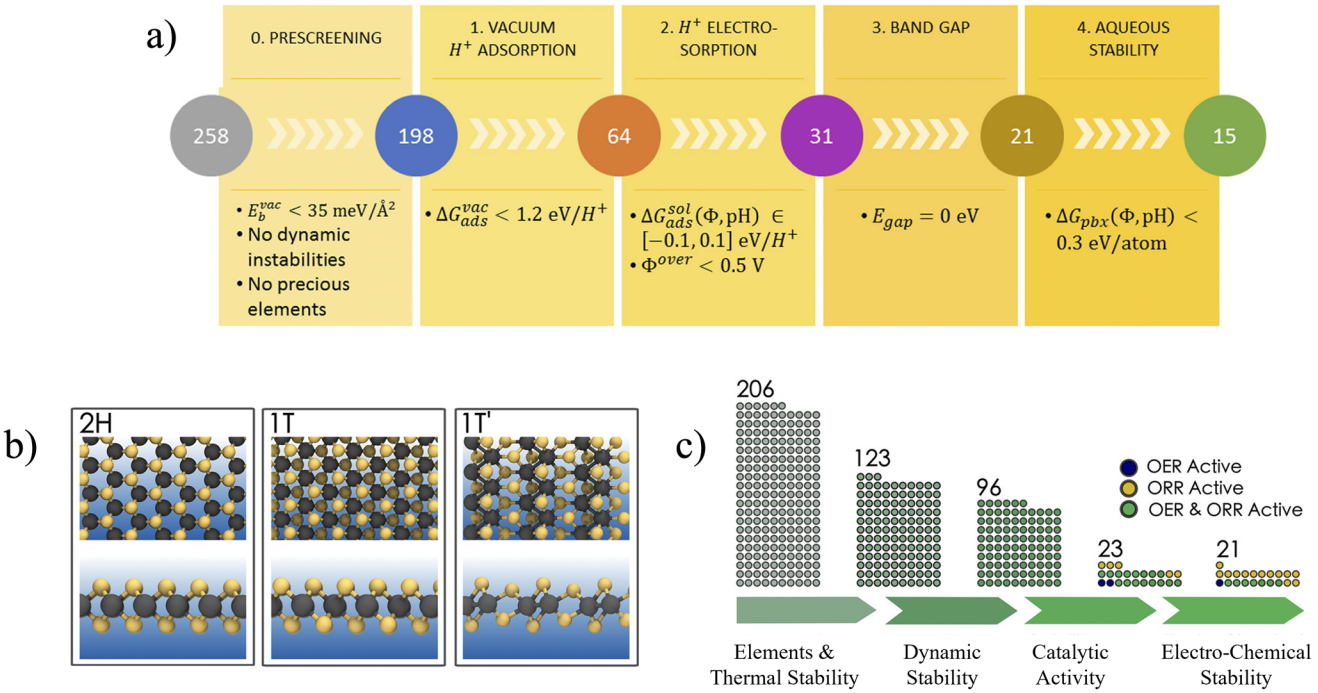

FIG. 9. (a) The computational workflow used to screen the best two-dimensional materials as electrocatalysts for HER, reproduced from Karmodak and Andreussi, ACS Energy Lett. **5**, 885–891 (2020). Copyright 2020 American Chemical Society. The criterion used to screen the materials has been shown in the bottom inset of each step, and the numbers shown in the circular inset correspond to materials screened in each step. (b) The transition metal dichalcogenide (TMDCs) structures considered for screening electrocatalysts for OER and ORR in Ref. 74 (c) The computational screening workflow used to screen the TMDCs for their activity and stability for OER and ORR in Ref. 74. The figure is reprinted with permission from Karmodak, Bursi, and Andreussi, J. Phys. Chem. Lett. **13**, 58–65 (2021). Copyright 2021 American Chemical Society.

around 2000 atoms for extended time scales (~50–80 ps), hydrogen bonding configurations, density profiles, and residence times of water molecules are effectively visualized. In addition to metal surfaces, the metal oxide/water interface is also simulated using the committee Neural Network Potential (c-NNPs) developed from Behler–Parrinello NNPs.[177,178]

Besides the neural network potentials, the Gaussian approximation potentials (GAPs) has been used as an efficient tool to model the inter-atomic interactions.[179] In this framework, the system energy and forces of the atoms interacting with each other is learned as a function of the atomic positions, determined from the pre-computed training dataset using the DFT calculations. A non-parametric kernel regression of the potential energy surface is performed to estimate the local energy using the local atomic environment as the descriptors. In comparison to the NN potentials, GAP could produce more accurate results as these potentials are not constrained to specific mathematical forms and flexibly readjusted to the training data.[180–182] Therefore, these potentials would be very efficient in reproducing different chemical environment and simulations for bond-making and breaking processes. However, studies with the electrochemical computations with GAP has not been performed extensively. This is particularly because of the complex nature of the electrochemical interfaces, and diverse sample space of solvent molecules at the interfaces lead to large data set for accurate performance. The effective modeling of electrochemical interfaces with GAP is an area with several new questions and great research opportunity.

Figure 11 summarizes the current challenges in electrochemical simulations and efforts made in recent years with ML and AI to address these issues. It is indeed evident that ML potentials have enabled studying an extended number of systems for larger timescales and great variations in the structural configurations. However, ML potentials show a few limitations. One of the major limitations is the ineffective modeling of the electrostatic effects at the electrified electrode/solvent interfaces and defining the pH or electrode potential dependence on the reaction thermodynamics.[152] These effects are important for polarized systems and electrochemical activity determination. Since most of the ML methods discussed earlier rely on the inter-atomic interactions with fixed cut-off radius, the long-range physical effects are neglected.[183] To this extent, the smooth overlap atomic positions (SOAP) descriptors have been used to capture the non-local interactions between water and charged electrode surfaces.[184]

In the traditional ML framework, the descriptors used for defining the potential energy surfaces are bound to two-body, three-body, or a hand-full of descriptors, such as the bond lengths, bond angles, and dihedral angle. Developing ML potentials with transferable applicability, particularly for electrochemical simulations, the many-body descriptor-based ML framework would be optimum.[185] Within the SOAP approach, the atomic environments are encoded using

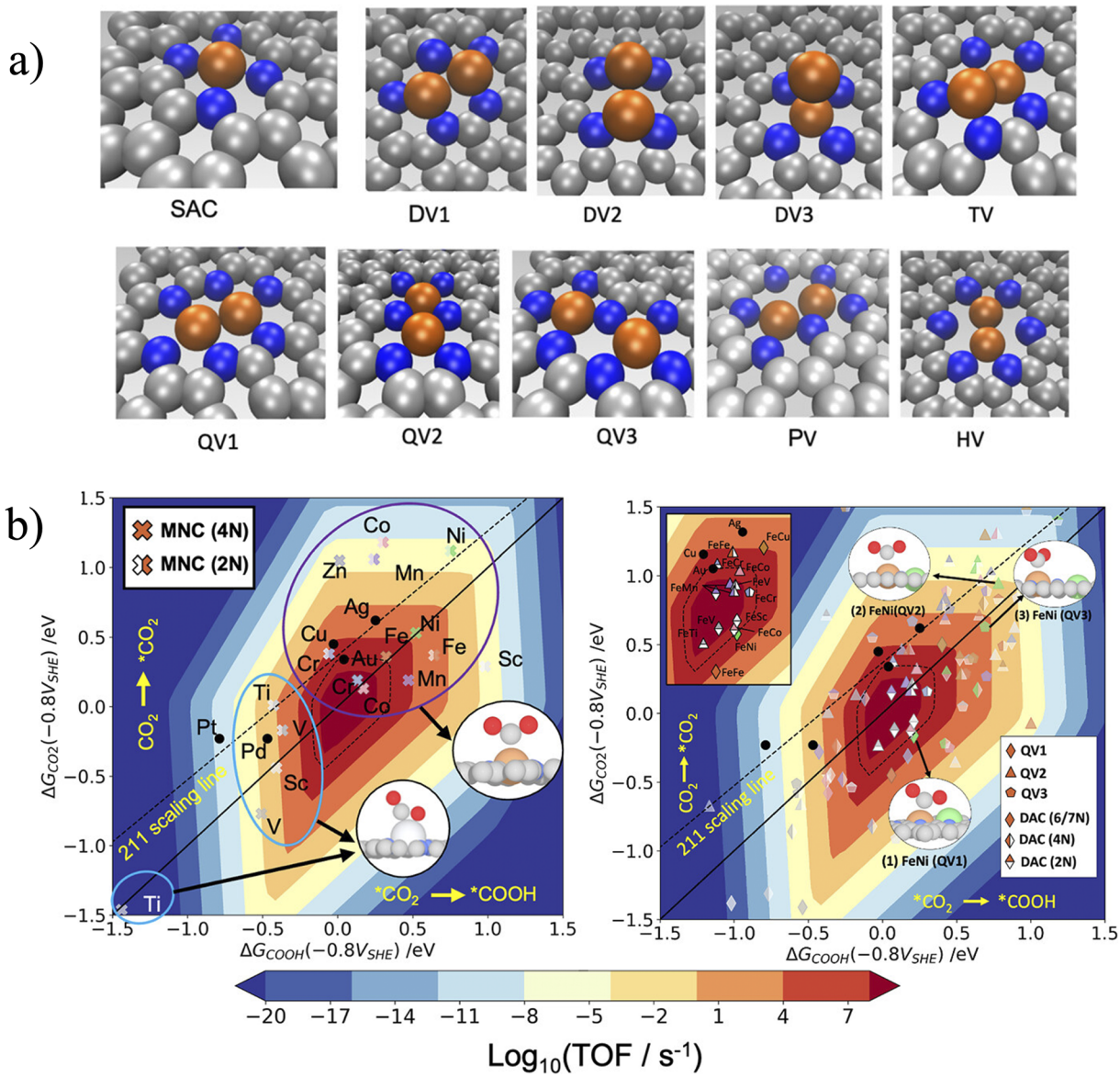

FIG. 10. The computational screening of single and diatom catalysts for CO_2 to CO reduction reactions. (a) shows the single (SAC) and di-atom catalyst structures considered for the study. The SAC is modeled by doping a single metal atom on di-atom carbon vacancy sites on a defected nitrogenated graphene sheet. The di-atom catalyst structures are obtained by doping two metal atoms on different vacancy sites varying from two to six carbon atoms. (b) The unified activity volcano plots for CO_2 to CO reduction reactions. The black dotted lines show the scaling lines for metal (211) surfaces. The different binding motifs for CO_2 are shown in the figure inset. The figures are reproduced with permission from Karmodak, ACS Catal. **12**, 4818–4824 (2022). Copyright 2022 American Chemical Society.

the rotationally invariant representations that use smoothed out atomic position vectors, mapped into coefficients of orthonormal basis functions.[186] These many-body descriptors enable measuring the similarity between atomic environments and allow mapping the local atomic environment very accurately. SOAP descriptors combined with different ML potentials could enable defining both the long-range and short-range interactions. In combination with GAP formulations, SOAP has allowed performing cohesive energy calculations of bulk systems, molecular dynamics simulations of large and complex systems, etc.[185]

A few kernel methods combined with the SOAP descriptors have been used to improve the accuracy and efficiency of simulations of electrochemical interfaces. A notable one corresponds to combining SOAP descriptors with long-distance equivariant representation (LODE) to enable defining the non-local dielectric responses at the electrochemical interfaces.[184] An atom density function is introduced, which depends upon the atomic positions both in the vicinity and far-off. Unlike the analytical force field methods, SOAP-based GAPs are computationally expensive.[152] LODE + SOAP is found to be more efficient and less expensive than the SOAP approach

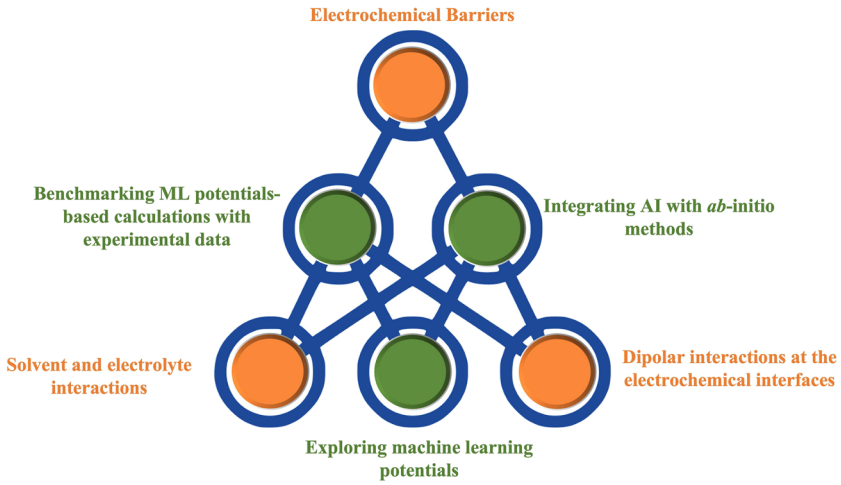

FIG. 11. The orange nodes denote the current challenges in electrochemical simulations; calculation of electrochemical barriers, defining solvent, and electrolyte interactions at the electrochemical interfaces and capturing the dipolar interactions in adsorbate energetics. The green nodes provide a possible way out employing the machine learning methods. Exploring ML potentials and benchmarking with the existing theoretical and experimental data might allow us to address a few or all of these challenges.

when used for evaluating the liquid water dielectric responses. However, the SOAP + LODE combination is found to be unsuitable for calculating dielectric responses at the electrified periodic boundaries.

Recently studies are ongoing to overcome the limitations of the SOAP descriptors for periodic systems and predict better ML models to capture the dipolar interactions at the electrochemical interfaces. Furthermore, calculations of the electrochemical barriers have been one of the greatest challenging tasks. The ML methods could be very handful for electrochemical barrier calculations; however, it would require a large number of training datasets. Combining the thermodynamic simulation schemes discussed earlier along with the scaling relationships (between the electrochemical thermodynamic free energies and kinetic barrier) might open up an effective way to develop ML methods to characterize the electrochemical barriers. Alternatively, benchmarking the ML potentials and artificial intelligence techniques with experimental data could give a solution to this and help in enhancing the accuracy and efficiency of these ML-based computational methods.

ACKNOWLEDGMENTS

N.K., V.M., and S.S. acknowledge the Shiv Nadar Institution of Eminence and Shiv Nadar Foundation for financial assistance and computational support for this project. O.A. acknowledges support from the National Science Foundation under Grant No. 1945139. F.B. acknowledges support from the American Chemical Society Petroleum Research Fund.

AUTHOR DECLARATIONS

Conflict of Interest

The authors have no conflicts to disclose.

Author Contributions

Vasanthapandiyan M: Data curation (equal); Formal analysis (equal); Funding acquisition (equal); Investigation (equal); Resources (equal); Visualization (equal); Writing – original draft (equal); Writing – review & editing (equal). **Shagun Singh**: Data curation (equal); Formal analysis (equal); Funding acquisition (equal); Resources (equal); Writing – original draft (equal); Writing – review & editing (equal). **Fernanda Bononi**: Data curation (equal); Formal analysis (equal); Resources (equal); Writing – original draft (equal); Writing – review & editing (equal). **Oliviero Andreussi**: Conceptualization (equal); Data curation (equal); Formal analysis (equal); Funding acquisition (equal); Methodology (equal); Resources (equal); Supervision (equal); Writing – original draft (equal); Writing – review & editing (equal). **Naiwrit Karmodak**: Conceptualization (lead); Data curation (lead); Formal analysis (lead); Funding acquisition (lead); Methodology (lead); Project administration (lead); Resources (lead); Supervision (lead); Visualization (lead); Writing – original draft (lead); Writing – review & editing (lead).

DATA AVAILABILITY

The data that support the findings of this study are available from the corresponding author upon reasonable request.

REFERENCES

[1] J. A. Turner, "Sustainable hydrogen production," Science **305**, 972–974 (2004).
[2] S. Chu and A. Majumdar, "Opportunities and challenges for a sustainable energy future," Nature **488**, 294–303 (2012).
[3] N. S. Lewis and D. G. Nocera, "Powering the planet: Chemical challenges in solar energy utilization," Proc. Natl. Acad. Sci. U. S. A. **103**, 15729–15735 (2006).

[4]J. M. Campos-Martin, G. Blanco-Brieva, and J. L. Fierro, "Hydrogen peroxide synthesis: An outlook beyond the anthraquinone process," Angew. Chem., Int. Ed. **45**, 6962–6984 (2006).
[5]G. A. Olah, "Beyond oil and gas: The methanol economy," Angew. Chem., Int. Ed. **44**, 2636–2639 (2005).
[6]S. Chu, Y. Cui, and N. Liu, "The path towards sustainable energy," Nat. Mater. **16**, 16–22 (2017).
[7]Z. W. Seh, J. Kibsgaard, C. F. Dickens, I. Chorkendorff, J. K. Nørskov, and T. F. Jaramillo, "Combining theory and experiment in electrocatalysis: Insights into materials design," Science **355**, eaad4998 (2017).
[8]M. K. Debe, "Electrocatalyst approaches and challenges for automotive fuel cells," Nature **486**, 43–51 (2012).
[9]B. C. Steele and A. Heinzel, "Materials for fuel-cell technologies," Nature **414**, 345–352 (2001).
[10]M. Graetzel, "Artificial photosynthesis: Water cleavage into hydrogen and oxygen by visible light," Acc. Chem. Res. **14**, 376–384 (1981).
[11]A. J. Bard and M. A. Fox, "Artificial photosynthesis: Solar splitting of water to hydrogen and oxygen," Acc. Chem. Res. **28**, 141–145 (1995).
[12]S. Nitopi, E. Bertheussen, S. B. Scott, X. Liu, A. K. Engstfeld, S. Horch, B. Seger, I. E. Stephens, K. Chan, C. Hahn *et al.*, "Progress and perspectives of electrochemical CO_2 reduction on copper in aqueous electrolyte," Chem. Rev. **119**, 7610–7672 (2019).
[13]C. G. Vayenas, R. E. White, and M. E. Gamboa-Aldeco, *Modern Aspects of Electrochemistry 42* (Springer Science & Business Media, 2008), Vol. 42.
[14]J. O. Bockris and T. N. Veziroglu, "Estimates of the price of hydrogen as a medium for wind and solar sources," Int. J. Hydrogen Energy **32**, 1605–1610 (2007).
[15]J. O. Bockris, "Hydrogen no longer a high cost solution to global warming: New ideas," Int. J. Hydrogen Energy **33**, 2129–2131 (2008).
[16]M. Gattrell, N. Gupta, and A. Co, "A review of the aqueous electrochemical reduction of CO_2 to hydrocarbons at copper," J. Electroanal. Chem. **594**, 1–19 (2006).
[17]A. D. Handoko, F. Wei, Jenndy, B. S. Yeo, and Z. W. Seh, "Understanding heterogeneous electrocatalytic carbon dioxide reduction through operando techniques," Nat. Catal. **1**, 922–934 (2018).
[18]J. Greeley, T. F. Jaramillo, J. Bonde, I. Chorkendorff, and J. K. Nørskov, "Computational high-throughput screening of electrocatalytic materials for hydrogen evolution," Nat. Mater. **5**, 909–913 (2006).
[19]Y. Chen, C. W. Li, and M. W. Kanan, "Aqueous CO_2 reduction at very low overpotential on oxide-derived Au nanoparticles," J. Am. Chem. Soc. **134**, 19969–19972 (2012).
[20]J. Luo, J.-H. Im, M. T. Mayer, M. Schreier, M. K. Nazeeruddin, N.-G. Park, S. D. Tilley, H. J. Fan, and M. Grätzel, "Water photolysis at 12.3% efficiency via perovskite photovoltaics and earth-abundant catalysts," Science **345**, 1593–1596 (2014).
[21]Y.-F. Li and A. Selloni, "Mechanism and activity of water oxidation on selected surfaces of pure and Fe-doped NiO_x," ACS Catal. **4**, 1148–1153 (2014).
[22]K. A. Stoerzinger, L. Qiao, M. D. Biegalski, and Y. Shao-Horn, "Orientation-dependent oxygen evolution activities of rutile IrO_2 and RuO_2," J. Phys. Chem. Lett. **5**, 1636–1641 (2014).
[23]Y. Lee, J. Suntivich, K. J. May, E. E. Perry, and Y. Shao-Horn, "Synthesis and activities of rutile IrO_2 and RuO_2 nanoparticles for oxygen evolution in acid and alkaline solutions," J. Phys. Chem. Lett. **3**, 399–404 (2012).
[24]J. Greeley, "Theoretical heterogeneous catalysis: Scaling relationships and computational catalyst design," Annu. Rev. Chem. Biomol. Eng. **7**, 605–635 (2016).
[25]J. K. Nørskov, F. Abild-Pedersen, F. Studt, and T. Bligaard, "Density functional theory in surface chemistry and catalysis," Proc. Natl. Acad. Sci. U. S. A. **108**, 937–943 (2011).
[26]J. H. Montoya, L. C. Seitz, P. Chakthranont, A. Vojvodic, T. F. Jaramillo, and J. K. Nørskov, "Materials for solar fuels and chemicals," Nat. Mater. **16**, 70–81 (2017).
[27]J. Rossmeisl, E. Skúlason, M. E. Björketun, V. Tripkovic, and J. K. Nørskov, "Modeling the electrified solid–liquid interface," Chem. Phys. Lett. **466**, 68–71 (2008).
[28]N. Marzari, A. Ferretti, and C. Wolverton, "Electronic-structure methods for materials design," Nat. Mater. **20**, 736–749 (2021).
[29]J. A. Gauthier, S. Ringe, C. F. Dickens, A. J. Garza, A. T. Bell, M. Head-Gordon, J. K. Nørskov, and K. Chan, "Challenges in modeling electrochemical reaction energetics with polarizable continuum models," ACS Catal. **9**, 920–931 (2018).
[30]M. Sprik, J. Hutter, and M. Parrinello, "*Ab initio* molecular dynamics simulation of liquid water: Comparison of three gradient-corrected density functionals," J. Chem. Phys. **105**, 1142–1152 (1996).
[31]O. Andreussi and G. Fisicaro, "Continuum embeddings in condensed-matter simulations," Int. J. Quantum Chem. **119**, e25725 (2019).
[32]B. Mennucci, E. Cances, and J. Tomasi, "Evaluation of solvent effects in isotropic and anisotropic dielectrics and in ionic solutions with a unified integral equation method: Theoretical bases, computational implementation, and numerical applications," J. Phys. Chem. B **101**, 10506–10517 (1997).
[33]J. Tomasi and M. Persico, "Molecular interactions in solution: An overview of methods based on continuous distributions of the solvent," Chem. Rev. **94**, 2027–2094 (1994).
[34]C. J. Cramer and D. G. Truhlar, "SMx continuum models for condensed phases," in *Trends and Perspectives in Modern Computational Science* edited by G. Maroulis and T. E. Simos, (Brill Academic, Amsterdam, 2006), Vol. 6, pp. 112–140.
[35]K. Reuter, "Ab initio thermodynamics and first-principles microkinetics for surface catalysis," Catal. Lett. **146**, 541–563 (2016).
[36]K. Reuter and M. Scheffler, "Composition, structure, and stability of RuO_2 (110) as a function of oxygen pressure," Phys. Rev. B **65**, 035406 (2001).
[37]J. K. Nørskov, J. Rossmeisl, A. Logadottir, L. Lindqvist, J. R. Kitchin, T. Bligaard, and H. Jonsson, "Origin of the overpotential for oxygen reduction at a fuel-cell cathode," J. Phys. Chem. B **108**, 17886–17892 (2004).
[38]N. G. Hörmann, O. Andreussi, and N. Marzari, "Grand canonical simulations of electrochemical interfaces in implicit solvation models," J. Chem. Phys. **150**, 041730 (2019).
[39]R. Sundararaman, W. A. Goddard, and T. A. Arias, "Grand canonical electronic density-functional theory: Algorithms and applications to electrochemistry," J. Chem. Phys. **146**, 114104 (2017).
[40]S. Ringe, N. G. Hormann, H. Oberhofer, and K. Reuter, "Implicit solvation methods for catalysis at electrified interfaces," Chem. Rev. **122**, 10777–10820 (2021).
[41]J. A. Gauthier, C. F. Dickens, H. H. Heenen, S. Vijay, S. Ringe, and K. Chan, "Unified approach to implicit and explicit solvent simulations of electrochemical reaction energetics," J. Chem. Theory Comput. **15**, 6895–6906 (2019).
[42]J. Tomasi, B. Mennucci, and R. Cammi, "Quantum mechanical continuum solvation models," Chem. Rev. **105**, 2999–3094 (2005).
[43]J.-L. Fattebert and F. Gygi, "Density functional theory for efficient *ab initio* molecular dynamics simulations in solution," J. Comput. Chem. **23**, 662–666 (2002).
[44]M. Cossi, G. Scalmani, N. Rega, and V. Barone, "New developments in the polarizable continuum model for quantum mechanical and classical calculations on molecules in solution," J. Chem. Phys. **117**, 43–54 (2002).
[45]S. Miertuš, E. Scrocco, and J. Tomasi, "Electrostatic interaction of a solute with a continuum. A direct utilizaion of AB initio molecular potentials for the prevision of solvent effects," Chem. Phys. **55**, 117–129 (1981).
[46]C. Amovilli, V. Barone, R. Cammi, E. Cancès, M. Cossi, B. Mennucci, C. S. Pomelli, and J. Tomasi, "Recent advances in the description of solvent effects with the polarizable continuum model," Adv. Quantum Chem. **32**, 227–261 (1998).
[47]M. Cossi and V. Barone, "Analytical second derivatives of the free energy in solution by polarizable continuum models," J. Chem. Phys. **109**, 6246–6254 (1998).
[48]R. Cammi and J. Tomasi, "Remarks on the use of the apparent surface charges (ASC) methods in solvation problems: Iterative versus matrix-inversion procedures and the renormalization of the apparent charges," J. Comput. Chem. **16**, 1449–1458 (1995).
[49]A. Klamt and G. Schüürmann, "COSMO: A new approach to dielectric screening in solvents with explicit expressions for the screening energy and its gradient," J. Chem. Soc., Perkin Trans. 2 **1993**, 799–805.
[50]A. Klamt, *COSMO-RS: From Quantum Chemistry to Fluid Phase Thermodynamics and Drug Design* (Elsevier, 2005).

[51]D. J. Giesen, C. J. Cramer, and D. G. Truhlar, "A semiempirical quantum mechanical solvation model for solvation free energies in all alkane solvents," J. Phys. Chem. **99**, 7137–7146 (1995).
[52]D. J. Giesen, M. Z. Gu, C. J. Cramer, and D. G. Truhlar, "A universal organic solvation model," J. Org. Chem. **61**, 8720–8721 (1996).
[53]D. J. Giesen, G. D. Hawkins, D. A. Liotard, C. J. Cramer, and D. G. Truhlar, "A universal model for the quantum mechanical calculation of free energies of solvation in non-aqueous solvents," Theor. Chem. Acc. **98**, 85–109 (1997).
[54]C. J. Cramer, D. G. Truhlar *et al.*, "Implicit solvation models: Equilibria, structure, spectra, and dynamics," Chem. Rev. **99**, 2161–2200 (1999).
[55]T. Zhu, J. Li, G. D. Hawkins, C. J. Cramer, and D. G. Truhlar, "Density functional solvation model based on CM2 atomic charges," J. Chem. Phys. **109**, 9117–9133 (1998).
[56]G. Fisicaro, L. Genovese, O. Andreussi, S. Mandal, N. N. Nair, N. Marzari, and S. Goedecker, "Soft-sphere continuum solvation in electronic-structure calculations," J. Chem. Theory Comput. **13**, 3829–3845 (2017).
[57]A. Klamt, B. Mennucci, J. Tomasi, V. Barone, C. Curutchet, M. Orozco, and F. J. Luque, "On the performance of continuum solvation methods. A comment on 'universal approaches to solvation modeling'," Acc. Chem. Res. **42**, 489–492 (2009).
[58]D. A. Scherlis, J.-L. Fattebert, F. Gygi, M. Cococcioni, and N. Marzari, "A unified electrostatic and cavitation model for first-principles molecular dynamics in solution," J. Chem. Phys. **124**, 074103 (2006).
[59]O. Andreussi, I. Dabo, and N. Marzari, "Revised self-consistent continuum solvation in electronic-structure calculations," J. Chem. Phys. **136**, 064102 (2012).
[60]K. Mathew, R. Sundararaman, K. Letchworth-Weaver, T. Arias, and R. G. Hennig, "Implicit solvation model for density-functional study of nanocrystal surfaces and reaction pathways," J. Chem. Phys. **140**, 084106 (2014).
[61]R. Sundararaman and W. A. Goddard, "The charge-asymmetric nonlocally determined local-electric (candle) solvation model," J. Chem. Phys. **142**, 064107 (2015).
[62]R. Sundararaman and K. Schwarz, "Evaluating continuum solvation models for the electrode-electrolyte interface: Challenges and strategies for improvement," J. Chem. Phys. **146**, 084111 (2017).
[63]C. Dupont, O. Andreussi, and N. Marzari, "Self-consistent continuum solvation (SCCS): The case of charged systems," J. Chem. Phys. **139**, 214110 (2013).
[64]O. Andreussi, N. G. Hormann, F. Nattino, G. Fisicaro, S. Goedecker, and N. Marzari, "Solvent-aware interfaces in continuum solvation," J. Chem. Theory Comput. **15**, 1996–2009 (2019).
[65]J. B. Foresman, T. A. Keith, K. B. Wiberg, J. Snoonian, and M. J. Frisch, "Solvent effects. 5. Influence of cavity shape, truncation of electrostatics, and electron correlation on ab initio reaction field calculations," J. Phys. Chem. **100**, 16098–16104 (1996).
[66]J.-L. Fattebert and F. Gygi, "First-principles molecular dynamics simulations in a continuum solvent," Int. J. Quantum Chem. **93**, 139–147 (2003).
[67]O. Andreussi, F. Nattino, and N. Georg Hörmann, "Continuum embedding models for electrolyte solutions in first-principles simulations of electrochemistry," in *Atomic-Scale Modelling of Electrochemical Systems* (John Wiley and Sons, 2021), pp. 93–137.
[68]F. Nattino, M. Truscott, N. Marzari, and O. Andreussi, "Continuum models of the electrochemical diffuse layer in electronic-structure calculations," J. Chem. Phys. **150**, 041722 (2019).
[69]N. Karmodak and O. Andreussi, "Catalytic activity and stability of two-dimensional materials for the hydrogen evolution reaction," ACS Energy Lett. **5**, 885–891 (2020).
[70]M. Truscott and O. Andreussi, "Field-aware interfaces in continuum solvation," J. Phys. Chem. B **123**, 3513–3524 (2019).
[71]C. P. Kelly, C. J. Cramer, and D. G. Truhlar, "Adding explicit solvent molecules to continuum solvent calculations for the calculation of aqueous acid dissociation constants," J. Phys. Chem. A **110**, 2493–2499 (2006).
[72]N. G. Hörmann, Z. Guo, F. Ambrosio, O. Andreussi, A. Pasquarello, and N. Marzari, "Absolute band alignment at semiconductor-water interfaces using explicit and implicit descriptions for liquid water," npj Comput. Mater. **5**, 100 (2019).
[73]L. Blumenthal, J. M. Kahk, R. Sundararaman, P. Tangney, and J. Lischner, "Energy level alignment at semiconductor–water interfaces from atomistic and continuum solvation models," RSC Adv. **7**, 43660–43670 (2017).
[74]N. Karmodak, L. Bursi, and O. Andreussi, "Oxygen evolution and reduction on two-dimensional transition metal dichalcogenides," J. Phys. Chem. Lett. **13**, 58–65 (2021).
[75]D. Beglov and B. Roux, "An integral equation to describe the solvation of polar molecules in liquid water," J. Phys. Chem. B **101**, 7821–7826 (1997).
[76]F. Hirata, *Molecular Theory of Solvation* (Springer Science & Business Media, 2003), Vol. 24.
[77]J. K. Percus and G. J. Yevick, "Analysis of classical statistical mechanics by means of collective coordinates," Phys. Rev. **110**, 1 (1958).
[78]J. Van Leeuwen, J. Groeneveld, and J. De Boer, "New method for the calculation of the pair correlation function. I," Physica **25**, 792–808 (1959).
[79]A. Kovalenko and F. Hirata, "Self-consistent description of a metal–water interface by the Kohn–Sham density functional theory and the three-dimensional reference interaction site model," J. Chem. Phys. **110**, 10095–10112 (1999).
[80]M. Otani and O. Sugino, "First-principles calculations of charged surfaces and interfaces: A plane-wave nonrepeated slab approach," Phys. Rev. B **73**, 115407 (2006).
[81]S. Nishihara and M. Otani, "Hybrid solvation models for bulk, interface, and membrane: Reference interaction site methods coupled with density functional theory," Phys. Rev. B **96**, 115429 (2017).
[82]I. Dabo, Y. Li, N. Bonnet, and N. Marzari, "Ab initio electrochemical properties of electrode surfaces," in *Fuel Cell Science: Theory, Fundamentals, and Biocatalysis* (Wiley, 2010), pp. 415–431.
[83]H. v. Helmholtz, "Ueber einige gesetze der vertheilung elektrischer ströme in körperlichen leitern, mit anwendung auf die thierisch-elektrischen versuche (schluss.)," Ann. Phys. **165**, 353–377 (1853).
[84]M. Gouy, "Sur la constitution de la charge électrique à la surface d'un électrolyte," J. Phys. Theor. Appl. **9**, 457–468 (1910).
[85]D. L. Chapman, "LI. A contribution to the theory of electrocapillarity," London, Edinburgh Dublin Philos. Mag. J. Sci. **25**, 475–481 (1913).
[86]D. Gunceler, K. Letchworth-Weaver, R. Sundararaman, K. A. Schwarz, and T. Arias, "The importance of nonlinear fluid response in joint density-functional theory studies of battery systems," Modell. Simul. Mater. Sci. Eng. **21**, 074005 (2013).
[87]I. Borukhov, D. Andelman, and H. Orland, "Steric effects in electrolytes: A modified Poisson-Boltzmann equation," Phys. Rev. Lett. **79**, 435 (1997).
[88]I. Borukhov, D. Andelman, and H. Orland, "Adsorption of large ions from an electrolyte solution: A modified Poisson–Boltzmann equation," Electrochim. Acta **46**, 221–229 (2000).
[89]S. Ringe, H. Oberhofer, C. Hille, S. Matera, and K. Reuter, "Function-space-based solution scheme for the size-modified Poisson–Boltzmann equation in full-potential DFT," J. Chem. Theory Comput. **12**, 4052–4066 (2016).
[90]S. Ringe, H. Oberhofer, and K. Reuter, "Transferable ionic parameters for first-principles Poisson-Boltzmann solvation calculations: Neutral solutes in aqueous monovalent salt solutions," J. Chem. Phys. **146**, 134103 (2017).
[91]O. Andreussi and N. Marzari, "Electrostatics of solvated systems in periodic boundary conditions," Phys. Rev. B **90**, 245101 (2014).
[92]R. Sundararaman, K. Letchworth-Weaver, K. A. Schwarz, D. Gunceler, Y. Ozhabes, and T. Arias, "JDFTx: Software for joint density-functional theory," SoftwareX **6**, 278–284 (2017).
[93]J. A. Gauthier, C. F. Dickens, S. Ringe, and K. Chan, "Practical considerations for continuum models applied to surface electrochemistry," ChemPhysChem **20**, 3074–3080 (2019).
[94]A. Ben-Naim, *Molecular Theory of Solutions* (OUP Oxford, 2006).
[95]H. Weingärtner and A. Ben-Naim, *Solvation Thermodynamics* (Plenum Press, New York, 1987; 1989), p. 246.
[96]M. Cococcioni, F. Mauri, G. Ceder, and N. Marzari, "Electronic-enthalpy functional for finite systems under pressure," Phys. Rev. Lett. **94**, 145501 (2005).
[97]P. Atkins and J. de Paula, "Atkins," Phys. Chem. **8**, 798 (2006).
[98]W. M. Haynes, *CRC Handbook of Chemistry and Physics* (CRC Press, 2016).
[99]N. Marković and P. Ross, Jr., "Surface science studies of model fuel cell electrocatalysts," Surf. Sci. Rep. **45**, 117–229 (2002).

[100]N. M. Marković, R. R. Adžić, B. Cahan, and E. Yeager, "Structural effects in electrocatalysis: Oxygen reduction on platinum low index single-crystal surfaces in perchloric acid solutions," J. Electroanal. Chem. **377**, 249–259 (1994).
[101]K. A. Persson, B. Waldwick, P. Lazic, and G. Ceder, "Prediction of solid-aqueous equilibria: Scheme to combine first-principles calculations of solids with experimental aqueous states," Phys. Rev. B **85**, 235438 (2012).
[102]M. Karamad, H. A. Hansen, J. Rossmeisl, and J. K. Nørskov, "Mechanistic pathway in the electrochemical reduction of CO_2 on RuO_2," ACS Catal. **5**, 4075–4081 (2015).
[103]L. D. Chen, M. Urushihara, K. Chan, and J. K. Nørskov, "Electric field effects in electrochemical CO_2 reduction," ACS Catal. **6**, 7133–7139 (2016).
[104]J. H. Montoya, C. Tsai, A. Vojvodic, and J. K. Nørskov, "The challenge of electrochemical ammonia synthesis: A new perspective on the role of nitrogen scaling relations," ChemSusChem **8**, 2180–2186 (2015).
[105]S. A. Akhade, R. M. Nidzyn, G. Rostamikia, and M. J. Janik, "Using Brønsted-Evans-Polanyi relations to predict electrode potential-dependent activation energies," Catal. Today **312**, 82–91 (2018).
[106]H. Xiao, T. Cheng, W. A. Goddard, and R. Sundararaman, "Mechanistic explanation of the pH dependence and onset potentials for hydrocarbon products from electrochemical reduction of CO on Cu (111)," J. Am. Chem. Soc. **138**, 483–486 (2016).
[107]K. J. P. Schouten, E. P. Gallent, and M. T. M. Koper, "The influence of pH on the reduction of CO and CO_2 to hydrocarbons on copper electrodes," J. Electroanal. Chem. **716**, 53–57 (2014).
[108]S. N. Steinmann and P. Sautet, "Assessing a first-principles model of an electrochemical interface by comparison with experiment," J. Phys. Chem. C **120**, 5619–5623 (2016).
[109]H. O. Stern, "Zur theorie der elektrolytischen doppelschicht," Z. Elektrochem. Angew. Phys. Chem. **30**, 508–516 (1924).
[110]H. Helmholtz, "Ueber einige gesetze der vertheilung elektrischer ströme in körperlichen leitern mit anwendung auf die thierisch-elektrischen versuche," Ann. Phys. Chem. **165**, 211–233 (1853).
[111]E. Skúlason, G. S. Karlberg, J. Rossmeisl, T. Bligaard, J. Greeley, H. Jónsson, and J. K. Nørskov, "Density functional theory calculations for the hydrogen evolution reaction in an electrochemical double layer on the pt(111) electrode," Phys. Chem. Chem. Phys. **9**, 3241–3250 (2007).
[112]E. R. Kötz, H. Neff, and K. Müller, "A UPS, XPS and work function study of emersed silver, platinum and gold electrodes," J. Electroanal. Chem. Interfacial Electrochem. **215**, 331–344 (1986).
[113]J. E. B. Randles, "The real hydration energies of ions," Trans. Faraday Soc. **52**, 1573–1581 (1956).
[114]K. Chan and J. K. Nørskov, "Electrochemical barriers made simple," J. Phys. Chem. Lett. **6**, 2663–2668 (2015).
[115]N. G. Hörmann, N. Marzari, and K. Reuter, "Electrosorption at metal surfaces from first principles," npj Computat. Mater. **6**, 136 (2020).
[116]M. M. Melander, "Grand canonical ensemble approach to electrochemical thermodynamics, kinetics, and model Hamiltonians," Curr. Opin. Electrochem. **29**, 100749 (2021).
[117]G. Kastlunger, P. Lindgren, and A. A. Peterson, "Controlled-potential simulation of elementary electrochemical reactions: Proton discharge on metal surfaces," J. Phys. Chem. C **122**, 12771–12781 (2018).
[118]P. Lindgren, G. Kastlunger, and A. A. Peterson, "Electrochemistry from the atomic scale, in the electronically grand-canonical ensemble," J. Chem. Phys. **157**, 180902 (2022).
[119]R. Parsons, "General equations for the kinetics of electrode processes," Trans. Faraday Soc. **47**, 1332–1344 (1951).
[120]K. S. Exner, "Why approximating electrocatalytic activity by a single free-energy change is insufficient," Electrochim. Acta **375**, 137975 (2021).
[121]K. S. Exner and H. Over, "Kinetics of electrocatalytic reactions from first-principles: A critical comparison with the ab initio thermodynamics approach," Acc. Chem. Res. **50**, 1240–1247 (2017).
[122]K. S. Exner, "A universal descriptor for the screening of electrode materials for multiple-electron processes: Beyond the thermodynamic overpotential," ACS Catal. **10**, 12607–12617 (2020).
[123]K. S. Exner, "Activity-stability volcano plots for material optimization in electrocatalysis," ChemCatChem **11**, 3234–3241 (2019).
[124]F. Abild-Pedersen, J. Greeley, F. Studt, J. Rossmeisl, T. R. Munter, P. G. Moses, E. Skulason, T. Bligaard, and J. K. Nørskov, "Scaling properties of adsorption energies for hydrogen-containing molecules on transition-metal surfaces," Phys. Rev. Lett. **99**, 016105 (2007).
[125]A. Logadottir, T. H. Rod, J. K. Nørskov, B. Hammer, S. Dahl, and C. Jacobsen, "The Brønsted–Evans–Polanyi relation and the volcano plot for ammonia synthesis over transition metal catalysts," J. Catal. **197**, 229–231 (2001).
[126]A. Michaelides, Z.-P. Liu, C. Zhang, A. Alavi, D. A. King, and P. Hu, "Identification of general linear relationships between activation energies and enthalpy changes for dissociation reactions at surfaces," J. Am. Chem. Soc. **125**, 3704–3705 (2003).
[127]S. Wang, V. Petzold, V. Tripkovic, J. Kleis, J. G. Howalt, E. Skulason, E. Fernández, B. Hvolbæk, G. Jones, A. Toftelund *et al.*, "Universal transition state scaling relations for (de)hydrogenation over transition metals," Phys. Chem. Chem. Phys. **13**, 20760–20765 (2011).
[128]J. K. Nørskov, T. Bligaard, J. Rossmeisl, and C. H. Christensen, "Towards the computational design of solid catalysts," Nat. Chem. **1**, 37–46 (2009).
[129]S. B. Vendelbo, C. F. Elkjær, H. Falsig, I. Puspitasari, P. Dona, L. Mele, B. Morana, B. Nelissen, R. Van Rijn, J. Creemer *et al.*, "Visualization of oscillatory behaviour of Pt nanoparticles catalysing CO oxidation," Nat. Mater. **13**, 884–890 (2014).
[130]R. B. Rankin and J. Greeley, "Trends in selective hydrogen peroxide production on transition metal surfaces from first principles," ACS Catal. **2**, 2664–2672 (2012).
[131]A. J. Medford, C. Shi, M. J. Hoffmann, A. C. Lausche, S. R. Fitzgibbon, T. Bligaard, and J. K. Nørskov, "CatMAP: A software package for descriptor-based microkinetic mapping of catalytic trends," Catal. Lett. **145**, 794–807 (2015).
[132]H. Falsig, J. Shen, T. S. Khan, W. Guo, G. Jones, S. Dahl, and T. Bligaard, "On the structure sensitivity of direct no decomposition over low-index transition metal facets," Top. Catal. **57**, 80–88 (2014).
[133]A. Vojvodic, A. J. Medford, F. Studt, F. Abild-Pedersen, T. S. Khan, T. Bligaard, and J. Nørskov, "Exploring the limits: A low-pressure, low-temperature Haber–Bosch process," Chem. Phys. Lett. **598**, 108–112 (2014).
[134]G. Jones, T. Bligaard, F. Abild-Pedersen, and J. K. Nørskov, "Using scaling relations to understand trends in the catalytic activity of transition metals," J. Phys.: Condens. Matter **20**, 064239 (2008).
[135]V. Viswanathan, H. A. Hansen, J. Rossmeisl, and J. K. Nørskov, "Universality in oxygen reduction electrocatalysis on metal surfaces," ACS Catal. **2**, 1654–1660 (2012).
[136]H. A. Hansen, V. Viswanathan, and J. K. Nørskov, "Unifying kinetic and thermodynamic analysis of 2 e^- and 4 e^- reduction of oxygen on metal surfaces," J. Phys. Chem. C **118**, 6706–6718 (2014).
[137]C. F. Dickens, C. Kirk, and J. K. Nørskov, "Insights into the electrochemical oxygen evolution reaction with ab initio calculations and microkinetic modeling: Beyond the limiting potential volcano," J. Phys. Chem. C **123**, 18960–18977 (2019).
[138]J. A. Gauthier, C. F. Dickens, L. D. Chen, A. D. Doyle, and J. K. Nørskov, "Solvation effects for oxygen evolution reaction catalysis on IrO_2(110)," J. Phys. Chem. C **121**, 11455–11463 (2017).
[139]A. Kulkarni, S. Siahrostami, A. Patel, and J. K. Nørskov, "Understanding catalytic activity trends in the oxygen reduction reaction," Chem. Rev. **118**, 2302–2312 (2018).
[140]A. R. Zeradjanin, P. Narangoda, J. Masa, and R. Schlögl, "What controls activity trends of electrocatalytic hydrogen evolution reaction? Activation energy *versus* frequency factor," ACS Catal. **12**, 11597–11605 (2022).
[141]A. Jain, Z. Wang, and J. K. Nørskov, "Stable two-dimensional materials for oxygen reduction and oxygen evolution reactions," ACS Energy Lett. **4**, 1410–1411 (2019).
[142]M. Pourbaix, *Atlas of Electrochemical Equilibria in Aqueous Solutions* (NACE, 1966).
[143]N. Takeno, "Atlas of Eh-pH diagrams; geological survey of japan open file report no. 419, 2005," Google Scholar There is no corresponding record for this reference, 77–79.

[144]D. G. Brookins, *Eh-pH Diagrams for Geochemistry* (Springer Science & Business Media, 2012).
[145]A. K. Singh, L. Zhou, A. Shinde, S. K. Suram, J. H. Montoya, D. Winston, J. M. Gregoire, and K. A. Persson, "Electrochemical stability of metastable materials," Chem. Mater. **29**, 10159–10167 (2017).
[146]A. M. Patel, J. K. Nørskov, K. A. Persson, and J. H. Montoya, "Efficient Pourbaix diagrams of many-element compounds," Phys. Chem. Chem. Phys. **21**, 25323–25327 (2019).
[147]A. Jain, J. Montoya, S. Dwaraknath, N. E. Zimmermann, J. Dagdelen, M. Horton, P. Huck, D. Winston, S. Cholia, S. P. Ong *et al.*, "The materials project: Accelerating materials design through theory-driven data and tools," in *Handbook of Materials Modeling: Methods: Theory and Modeling* (Springer, 2020), pp. 1751–1784.
[148]N. Mounet, M. Gibertini, P. Schwaller, D. Campi, A. Merkys, A. Marrazzo, T. Sohier, I. E. Castelli, A. Cepellotti, G. Pizzi, and N. Marzari, "Two-dimensional materials from high-throughput computational exfoliation of experimentally known compounds," Nat. Nanotechnol. **13**, 246–252 (2018).
[149]S. Haastrup, M. Strange, M. Pandey, T. Deilmann, P. S. Schmidt, N. F. Hinsche, M. N. Gjerding, D. Torelli, P. M. Larsen, A. C. Riis-Jensen *et al.*, "The computational 2D materials database: High-throughput modeling and discovery of atomically thin crystals," 2D Mater. **5**, 042002 (2018).
[150]N. Karmodak, S. Vijay, G. Kastlunger, and K. Chan, "Computational screening of single and di-atom catalysts for electrochemical CO_2 reduction," ACS Catal. **12**, 4818–4824 (2022).
[151]O. T. Unke, S. Chmiela, H. E. Sauceda, M. Gastegger, I. Poltavsky, K. T. Schütt, A. Tkatchenko, and K.-R. Müller, "Machine learning force fields," Chem. Rev. **121**, 10142–10186 (2021).
[152]I. Poltavsky and A. Tkatchenko, "Machine learning force fields: Recent advances and remaining challenges," J. Phys. Chem. Lett. **12**, 6551–6564 (2021).
[153]M. Meuwly, "Machine learning for chemical reactions," Chem. Rev. **121**, 10218–10239 (2021).
[154]P. S. Rice, Z.-P. Liu, and P. Hu, "Hydrogen coupling on platinum using artificial neural network potentials and DFT," J. Phys. Chem. Lett. **12**, 10637–10645 (2021).
[155]L. Chen, X. Zhang, A. Chen, S. Yao, X. Hu, and Z. Zhou, "Targeted design of advanced electrocatalysts by machine learning," Chin. J. Catal. **43**, 11–32 (2022).
[156]T. Wen, C.-Z. Wang, M. J. Kramer, Y. Sun, B. Ye, H. Wang, X. Liu, C. Zhang, F. Zhang, K.-M. Ho, and N. Wang, "Development of a deep machine learning interatomic potential for metalloid-containing Pd-Si compounds," Phys. Rev. B **100**, 174101 (2019).
[157]N. Artrith, "Machine learning for the modeling of interfaces in energy storage and conversion materials," J. Phys.: Energy **1**, 032002 (2019).
[158]G. P. Pun, V. Yamakov, J. Hickman, E. Glaessgen, and Y. Mishin, "Development of a general-purpose machine-learning interatomic potential for aluminum by the physically informed neural network method," Phys. Rev. Mater. **4**, 113807 (2020).
[159]J. Behler, "Perspective: Machine learning potentials for atomistic simulations," J. Chem. Phys. **145**, 170901 (2016).
[160]A. P. Bartók, S. De, C. Poelking, N. Bernstein, J. R. Kermode, G. Csányi, and M. Ceriotti, "Machine learning unifies the modeling of materials and molecules," Sci. Adv. **3**, e1701816 (2017).
[161]F. Noé, A. Tkatchenko, K.-R. Müller, and C. Clementi, "Machine learning for molecular simulation," Annu. Rev. Phys. Chem. **71**, 361–390 (2020).
[162]J. Behler and G. Csányi, "Machine learning potentials for extended systems: A perspective," Eur. Phys. J. B **94**, 142 (2021).
[163]G. Montavon, M. Rupp, V. Gobre, A. Vazquez-Mayagoitia, K. Hansen, A. Tkatchenko, K.-R. Müller, and O. A. Von Lilienfeld, "Machine learning of molecular electronic properties in chemical compound space," New J. Phys. **15**, 095003 (2013).
[164]T. Bereau, D. Andrienko, and O. A. Von Lilienfeld, "Transferable atomic multipole machine learning models for small organic molecules," J. Chem. Theory Comput. **11**, 3225–3233 (2015).
[165]N. Artrith, T. Morawietz, and J. Behler, "High-dimensional neural-network potentials for multicomponent systems: Applications to zinc oxide," Phys. Rev. B **83**, 153101 (2011).
[166]S. A. Ghasemi, A. Hofstetter, S. Saha, and S. Goedecker, "Interatomic potentials for ionic systems with density functional accuracy based on charge densities obtained by a neural network," Phys. Rev. B **92**, 045131 (2015).
[167]X. Xie, K. A. Persson, and D. W. Small, "Incorporating electronic information into machine learning potential energy surfaces via approaching the ground-state electronic energy as a function of atom-based electronic populations," J. Chem. Theory Comput. **16**, 4256–4270 (2020).
[168]T. W. Ko, J. A. Finkler, S. Goedecker, and J. Behler, "A fourth-generation high-dimensional neural network potential with accurate electrostatics including non-local charge transfer," Nat. Commun. **12**, 398 (2021).
[169]K. T. Schütt, M. Gastegger, A. Tkatchenko, K.-R. Müller, and R. J. Maurer, "Unifying machine learning and quantum chemistry with a deep neural network for molecular wavefunctions," Nat. Commun. **10**, 5024 (2019).
[170]X. Zhang, Y. Tian, L. Chen, X. Hu, and Z. Zhou, "Machine learning: A new paradigm in computational electrocatalysis," J. Phys. Chem. Lett. **13**, 7920–7930 (2022).
[171]M. Kulichenko, J. S. Smith, B. Nebgen, Y. W. Li, N. Fedik, A. I. Boldyrev, N. Lubbers, K. Barros, and S. Tretiak, "The rise of neural networks for materials and chemical dynamics," J. Phys. Chem. Lett. **12**, 6227–6243 (2021).
[172]J. Behler and M. Parrinello, "Generalized neural-network representation of high-dimensional potential-energy surfaces," Phys. Rev. Lett. **98**, 146401 (2007).
[173]A. E. Mikkelsen, J. Schiøtz, T. Vegge, and K. W. Jacobsen, "Is the water/Pt (111) interface ordered at room temperature?," J. Chem. Phys. **155**, 224701 (2021).
[174]A. E. Mikkelsen, H. H. Kristoffersen, J. Schiøtz, T. Vegge, H. A. Hansen, and K. W. Jacobsen, "Structure and energetics of liquid water–hydroxyl layers on Pt(111)," Phys. Chem. Chem. Phys. **24**, 9885–9890 (2022).
[175]S. K. Natarajan and J. Behler, "Neural network molecular dynamics simulations of solid–liquid interfaces: Water at low-index copper surfaces," Phys. Chem. Chem. Phys. **18**, 28704–28725 (2016).
[176]S. Kondati Natarajan and J. Behler, "Self-diffusion of surface defects at copper–water interfaces," J. Phys. Chem. C **121**, 4368–4383 (2017).
[177]C. Schran, K. Brezina, and O. Marsalek, "Committee neural network potentials control generalization errors and enable active learning," J. Chem. Phys. **153**, 104105 (2020).
[178]P. Schienbein and J. Blumberger, "Nanosecond solvation dynamics of the hematite/liquid water interface at hybrid DFT accuracy using committee neural network potentials," Phys. Chem. Chem. Phys. **24**, 15365–15375 (2022).
[179]A. P. Bartók, M. C. Payne, R. Kondor, and G. Csányi, "Gaussian approximation potentials: The accuracy of quantum mechanics, without the electrons," Phys. Rev. Lett. **104**, 136403 (2010).
[180]X. Li, W. Paier, and J. Paier, "Machine learning in computational surface science and catalysis: Case studies on water and metal–oxide interfaces," Front. Chem. **8**, 601029 (2020).
[181]R. Jinnouchi, F. Karsai, and G. Kresse, "On-the-fly machine learning force field generation: Application to melting points," Phys. Rev. B **100**, 014105 (2019).
[182]R. Jinnouchi, J. Lahnsteiner, F. Karsai, G. Kresse, and M. Bokdam, "Phase transitions of hybrid perovskites simulated by machine-learning force fields trained on the fly with Bayesian inference," Phys. Rev. Lett. **122**, 225701 (2019).
[183]S. Yue, M. C. Muniz, M. F. Calegari Andrade, L. Zhang, R. Car, and A. Z. Panagiotopoulos, "When do short-range atomistic machine-learning models fall short?," J. Chem. Phys. **154**, 034111 (2021).
[184]A. Grisafi and M. Ceriotti, "Incorporating long-range physics in atomic-scale machine learning," J. Chem. Phys. **151**, 204105 (2019).
[185]M. A. Caro, "Optimizing many-body atomic descriptors for enhanced computational performance of machine learning based interatomic potentials," Phys. Rev. B **100**, 024112 (2019).
[186]A. P. Bartók, R. Kondor, and G. Csányi, "On representing chemical environments," Phys. Rev. B **87**, 184115 (2013).